Journal of the Geological Survey of Brazil

Hydrothermal alteration, mineralization and fluid inclusions in the Pista and Fofão prospects: implications for the genetic model of the Coringa polymetallic deposit, SE Tapajós Mineral Province, Amazonian Craton, Brazil

Rafael Guimarães Corrêa-Lima[1,2*], Evandro Luiz Klein[3,1,2]

[1] Programa de Pós-graduação em Geologia e Geoquímica, Instituto de Geociências, Universidade Federal do Pará - UFPA, Rua Augusto Corrêa s/n, Belém-PA, Brazil, CEP: 66075-110.
[2] Grupo de Pesquisa em de Geologia Econômica, Universidade Federal do Pará, Brazil.
[3] CPRM-Geological Survey of Brazil. SBN, Q2, Asa Norte, Brasília-DF, Brazil, CEP: 70040-904

Abstract

Pista and Fofão are prospects located near the main orebodies of the Coringa polymetallic deposit, in southeastern Tapajós Mineral Province of the Amazonian Craton. In both prospects, the mineralization is hosted in an Orosirian alkali feldspar granite, which is associated with coeval volcanic rocks at Pista. The paleo-hydrothermal system comprises an early post-magmatic stage, characterized by albite and K-feldspar alterations. Silicified and brecciated zones, sericitization of wall-rocks, both with adularia, as well as carbonatization (siderite and Mn-siderite rich stage) are the proximal ore alteration zones. Chlorite – hematite – rutile – epidote veinlets represent weak and distal zones of hydrothermal alteration. The mineralization is polymetallic (Au and subordinate Ag, Zn, Pb, and Cu) and occurs as dissemination and filling fissure veinlets. Gold occurs predominantly as Au-Ag-tellurides included in pyrite, and as free gold in association with pyrite, sphalerite and hematite within quartz veinlets. Fluid inclusions trapped in quartz veinlets show H_2O, H_2O-CO_2-NaCl and CO_2-only inclusions. Microthermometric data indicate an H_2O-CO_2-NaCl fluid, likely of magmatic derivation, with low-salinity (5.4 ± 1.3 wt. % NaCl equiv.) and moderate density (0.36-0.94 g/cm^3) trapped between 264 and 370ºC, and a low-salinity aqueous fluid (≤11.2 wt % NaCl equiv.) trapped at 280 to 360ºC, possibly evolved from effervescence followed by isothermal mixing with an external heated H_2O-NaCl fluid, probably meteoric. After this, the fluids were continuously diluted and cooled. This stage is represented by the liquid-rich H_2O-NaCl fluid inclusions of low salinity (up to 5.3 wt. % NaCl equiv.) and relatively low trapping temperature (177 to 113°C). The petrographic and fluid inclusions data suggest that the Au, Ag and base metals precipitation resulted from fluid mixing and dilution, which led to the breakdown of $Au(HS)_2^-$. We interpret the Pista and Fofão prospects as part of a magmatic-hydrothermal mineralized system, with some characteristics compa-tible with those of low- to intermediate-sulfidation epithermal systems, despite the absence of some typical textures from these systems..

Article Information

Publication type: Research paper
Received 29 June 2019
Accepted 1 April 2020
Online pub. 28 April 2020
Editor(s): Steffen Hagemann

Keywords:
Pista and Fofão
epithermal gold mineralization,
Tapajós, Brazil

*Corresponding author
Rafael Guimarães Corrêa-Lima
E-mail address:rg.correalima@gmail.com

1. Introduction

The Tapajós Mineral Province (TMP), south-central portion of the Amazonian Craton (Fig. 1A), is an important metallogenic province of Brazil. Unofficial data indicate that over 600 tons of gold have been extracted from alluvial sources during the first three decades of production (from ~1958). Between 1985 and 1995, about 90 tons of gold were produced, which were also extracted from supergene and hypogene sources (Klein and Carvalho 2008). In the last decade, mining companies have intensified exploration in both supergene and hypogene ore zones from a series of deposits, which include Tocantinzinho, Palito, São Chico, São Jorge, Cuiú-Cuiú, Ouro Roxo, and Coringa, and resources over 340 t Au have been defined (Fig. 1B).

This growing exploration interest turns the TMP into an important area for geological and metallogenic research at regional and local scales. Regionally, the definition of lithostratigraphic units, geochronological and geotectonic studies have been the main themes. Regional studies have involved isotopic (Santos et al. 2001; Lafon and Coutinho 2008) and structural approaches (Klein et al. 2002), focused on the establishment of the timing of mineralizing and geological events in the province. At the local scale, several authors have been concerned about the characterization of host rocks, hydrothermal alteration including metasomatic processes,

ISSN: 2595-1939
https://doi.org/10.29396/jgsb.2020.v3.n1.3
Open access at jgsb.cprm.gov.br

as well as the nature and evolution of the ore fluids and the proposition of genetic models for individual deposits (Dreher et al. 1998; Jacobi 1999; Juliani et al. 2002; Klein et al. 2004; Juliani et al. 2005; Borges et al. 2009; Souza 2009; Misas 2010; Veloso and Santos 2013; Santiago et al. 2013; Villas et al. 2013; Santos et al. 2013; Assunção and Klein 2014; Juliani et al. 2014; Guimarães et al. 2015; Tokashiki et al. 2015; Silva Júnior and Klein 2015; Queiroz and Villas 2015; Borgo et al. 2017; Cassini et al. 2017; Queiroz and Klein 2018; Biondi et al. 2018; Lopes and Moura 2019; Oliveira et al. 2019).

In this context, the Coringa deposit (845.000 t @ 7.95 g/t Au; 216 koz of Au; indicated resources – Gunnesh et al. 2019) and the southeastern part of the TMP became widely studied (e.g., Guimarães et al. 2015; Tokashiki et al. 2015; Corrêa Lima et al. 2014; Guimarães et al. 2019). According to these studies, the Coringa deposit has been interpreted as a low- to intermediate-sulfidation epithermal and polymetallic mineralization (Au-Ag-Pb-Zn-Cu; only the Au and Ag are considered economic/exploitable to date) and is hosted in the Paleoproterozoic volcano-plutonic association (~1.97 Ga). In order to understand the hydrothermal processes forming the Coringa deposit, this investigation provides new data about the ore, host rocks and their hydrothermal alterations in the Pista and Fofão prospects, which are satellite targets to the Coringa deposit. Additionally, we present new information about hydrothermal fluids based on a microthermometry study on fluid inclusions trapped in mineralized quartz veins.

2. Geological Setting

The TMP is included in the Tapajós Domain (Fig. 1B), in the southern Tapajós-Parima Province (2.10-1.87 Ga; Santos et al. 2000; Vasquez et al. 2008) of the Amazonian Craton. The tectonic evolution of the Tapajós Domain is still widely discussed and several models are proposed. According to Santos et al. (2000, 2001 and 2004), the Tapajós Domain was formed by accretionary events related to five 2.0-1.87 Ga magmatic arcs, involved in two orogenic cycles (2.04-1.95 Ga Mundurucus Orogeny and 1.9-1.88 Ga Tropas Orogeny) with SW-NE oriented subduction. Alternatively, a single orogenic event (Cuiú-Cuiú Orogeny), involving the evolution of an Orosirian magmatic arc (>1.95 Ga) with successive magmatic pulses in post-collisional, extensional and within plate conditions (~1.88 Ga Uatumã Event), was proposed by Vasquez et al. (2002, 2008) and Klein et al. (2012). Juliani et al. (2013) suggested that deep E-W regional structures, evidenced by magnetometry and gravimetric data, are continuous from eastern Amazonian Craton (Carajás region) to the TMP region, indicating accretionary processes by continental arcs with S-N oriented subduction. Teixeira et al. (2015) proposed that the Tapajós Domain is the result of wide, intracontinental magmatism by underplating processes in extensional setting.

The Castelo dos Sonhos Formation, located near the limits between Tapajós and Iriri-Xingu domains (Figure 1B) and recently included in the Tapajós Domain (Klein et al. 2017), comprises medium to coarse-grained meta-sandstones, meta-conglomerates with centimeter to meter quartz clasts, quartzites, BIF and schists, which hosts modified paleoplacer-type gold mineralization (Queiroz and Klein 2018). The meta-conglomerates have a maximum deposition age of 2050 Ma, whereas the meta-sandstones have maximum sedimentation ages of 2074, 2088 and 2104 Ma (Klein at al. 2017). These sedimentary rocks were intruded by granitoids with ages up to 2011 ± 6 Ma (Queiroz et al. 2015), which places the sedimentation of the Castelo dos Sonhos Formation between 2011 and 2050 Ma. Klein et al. (2017) argue that the Castelo dos Sonhos Formation is part of a larger foreland system related to Rhyacian orogenies in the eastern and northeastern Bacajá and Santana do Araguaia domains of the Amazonian Craton.

Episodes of siliciclastic, turbidite sedimentation in back-arc and oceanic plateau settings, and island arc-related volcanism generated pre-collisional associations of the Jacareacanga Group, which comprises mafic metavolcanic and ultramafic rocks at the base and metaturbidite, metasilexite, intercalated with quartzites and banded iron formations at the top, with detrital zircons of 2.07-2.01 Ga (Santos et al. 2000, 2001). Recently, Vasquez et al. (2019) obtained similar depositional ages (2.05-2.00 Ga) in detrital zircons from paragneisses and also defined a high-grade metamorphic event around 1.95 Ga, recorded by zircons in peraluminous (garnet-biotite-muscovite) leucogranitic veins. After, the evolution of the Orosirian magmatic arc (Cuiú-Cuiú Magmatic Arc) is marked by the emplacement of granitic and volcanic rocks of the Cuiú-Cuiú Complex, Comandante Arara Formation, Creporizão Intrusive Suite and Vila Riozinho Formation (Vasquez et al. 2008, 2014).

The Cuiú-Cuiú Complex (2033-2005 Ma) comprises orthogneisses (amphibolite facies) and partly deformed granitoids, mainly arc-related calc-alkaline granodiorites and tonalites (Vasquez et al. 2002, 2008; Santos et al. 2004). These rocks show positive and negative εNd values and TDM ages significantly older than the crystallization age, which is attributed to a continental arc configuration (Vasquez et al. 2014). These rocks host orogenic-type gold mineralization in the Patinhas prospect, in the southwestern Tapajós province (Klein et al. 2004). The effusive and eruptive volcanic rocks of the Comandante Arara Formation (2020-2012 Ma) are considered the extrusive correspondent of the Cuiú-Cuiú Complex (Vasquez et al. 2013).

The Creporizão Intrusive Suite is related to the late collisional period of the Cuiú-Cuiú Arc (Vasquez et al. 2002, 2008) or to a continental arc (Santos et al. 2004). This suite includes peraluminous calc-alkaline granitoids, crystallized between 1997 and 1957 Ma (Santos et al. 2001; Vasquez et al. 2002). They intrude into the Cuiú-Cuiú Complex along regional NW-SE striking shear zones, which host a large part of the mineralization in the Tapajós Province (Klein et al. 2002; Santos and Coutinho 2008). Deposits include the Cuiú-Cuiú goldfield (Assunção and Klein 2014; Silva Júnior and Klein 2015) and the Tocantinzinho gold deposit (Villas et al. 2013; Borgo et al. 2017). In the western TMP, high-K to shoshonitic, calc-alkaline volcanic rocks of the Vila Riozinho Formation crop out. These were formed between 2000 and 1998 Ma and are considered the correspondent volcanic rocks of the Creporizão Suite (Vasquez et al. 2002).

Plutonic events between ~1.90 and 1.88 Ga recorded in the rocks of the Tropas, Parauari and Ingarana suites are likely the representative rocks of either post-collisional phase of the Cuiú-Cuiú magmatic arc (Vasquez et al. 2008), or extensional magmatism not related to the orogeny but to the onset of the Uatumã SLIP - Silicic Large Igneous Province (Klein et al. 2012, 2017). The Tropas Suite comprises calc-alkaline tonalites to granodiorites with ages of 1907 and 1892 Ma (Santos et al. 2001, 2004), which are the host rocks of the Ouro Roxo deposit (Veloso and Santos 2013). The Parauari

Suite is composed of high-K, calc-alkaline granodiorites and diorites (Vasquez et al. 2002, 2008) with crystallization ages around 1883 Ma (Santos et al. 2000). The 1881-1878 Ga gabbroic rocks of the Ingarana Suite represent the mafic magmatism associated with the Parauari felsic magmatism (Vasquez et al. 2002, 2008).

The Parauari magmatism was accompanied and followed by extensional tectonic episodes, which led to the formation of plutono-volcanic associations, that include rocks of the Bom Jardim Formation (1881 Ma), the alkaline volcanic and pyroclastic rocks of the Iriri Group (1870 Ma) and the A-type granites of the Maloquinha Suite (1878 Ma). These last two units are related to the Uatumã SLIP (1.89-1.87 Ga). The volcanoclastic and epiclastic rocks of the Novo Progresso Formation are located spatially close to the Iriri Group and show a maximum depositional age of 1857 Ma, indicating a temporal relationship with the Uatumã SLIP (Klein et al. 2018).

The buildup of Statherian continental rifts (after 1800 Ma) resulted in episodes of siliciclastic sedimentation, recorded in sandstones and arkosic rocks of the Buiuçu Formation. The dikes and sills of the Crepori Diabase, typical continental tholeiitic basalts, intruded in the Buiuçu rocks and provided the minimum depositional age of 1780 Ma for the sedimentary rocks (Santos et al. 2002). The Porquinho Granite (1786 Ma) represents the latest plutonic magmatism of this rifting episode and Santos et al. (2004) suggested a correlation with the Teles Pires magmatism (1800-1772 Ma) in the Juruena Domain to the south (Fig. 1A).

3. Summary of the Coringa Deposit

The area of the Coringa deposit and of the satellite Pista and Fofão prospects is dominated by Paleoproterozoic felsic volcano-plutonic associations (Fig. 2A and 2B), formed by rhyolites, dacites, rhyodacites, latites, and andesites, as well as their pyroclastic components (ignimbrites, tuffs, and breccias) with ages of 1966 ± 6 Ma to 1989 ± 12 Ma (Tokashiki et al. 2015; Guimarães et al. 2019), which includes them in the Vila Riozinho Formation, as defined by Lamarão et al. (2002). Recently, Guimarães et al. (2019) described a magnetic pyroclastic facies in the region of the Coringa deposit. This facies consists of ignimbrites of rhyolitic composition and hydrothermally altered breccias. This volcanic sequence is intruded by the Serra Alkali Feldspar Granite dated at 1998 ± 6 Ma which makes it coeval with the granitoids of the Creporizão Intrusive Suite.

According to Tokashiki et al. (2015), the paleo-hydrothermal system of the Coringa deposit includes K-feldspar alteration (earlier and less intensive), propylitic, sericitic (with adularia), and argillic alterations, silicification, and carbonatization. According to these authors, gold mineralization is associated mostly with rhyolitic domes and expressed as sulfide-quartz veins, which contain galena, pyrite, sphalerite, gold, and silver. In the Mato Velho target, 20 km north of the Coringa deposit, Feio (2014) obtained a Pb-Pb model age of 1974 Ma in gold-related pyrite crystals in quartz veins hosted in dacites. These relationships suggest contemporaneity between gold mineralization and the emplacement of the volcanic host rocks.

4. Sampling and analytical procedures

For this research, samples of three drill holes were used. 37 polished thin sections were analyzed on a Zeiss Axioplan microscope adapted with transmitted and reflected lights. Sulfides, carbonates, and chlorite were analyzed using the scanning electron microscope (LEO-1430; Geosciences Institute, Universidade Federal do Pará). Polished thin sections were coated with carbon before BSE and EDS analyses. The analyses were conducted with constant accelerating voltage (20 kV), electron beam-induced current of 90 µA, working distance of 15 mm and 30 s for each analysis with 4,000 – 5,000 cycles. The fluid system was investigated by both petrographic and microthermometric analyses of groups of fluid inclusions trapped in quartz crystals of sulfide-quartz veins. The microthermometric study was carried out using a Linkam MDSG600 heating-freezing stage with a temperature range of −196 to 600°C coupled to an Axioskop 40 microscope with transmitted light, installed at the Fluid Inclusions Laboratory of Geoscience Institute – Universidade Federal do Pará, in Belém, Brazil. The calibration was done with synthetic fluid inclusions containing pure CO_2 (melting at -56.6 ºC) and H_2O (melting at 0.0 ºC). The precision is estimated at ±0.5º C and ±5º C for temperatures lower and higher than 50º C, respectively. The analytical procedures followed the fluid inclusion assemblage criteria (Goldstein and Reynolds 1994; Chi and Lu 2008). The salinity of aqueous and aqueous-carbonic inclusions (represented as % wt. NaCl equiv.) was estimated according to Bodnar (1993) and Collins (1979), respectively. Physical and chemical properties, such as density and composition (mole fraction) were estimated with the software FLINCOR (Brown 1989), following the equations of Brown and Lamb (1986) for H_2O and CO_2 only inclusions, and Bowers and Helgeson (1983) for H_2O-CO_2-NaCl inclusions.

5. The Pista and Fofão prospects

5.1. Host roscks

The main host rock of gold mineralization in the Pista and Fofão prospects is an alkali feldspar granite related to a calc-alkaline granitic body (1998 ± 6 Ma), defined as the Serra Alkali Feldspar Granite (Guimarães et al. 2019). In addition, a few subordinate volcanic rocks and hydrothermal breccias were recognized (Fig. 3).

5.1.1. Alkali feldspar granite

The alkali feldspar granite is isotropic, medium-grained, hololeucocratic (M'< 5), with pinkish to reddish colors (Fig. 4A) and granular hypidiomorphic, granophyric and micrographic textures (Fig. 4F). In some samples, an evolution from granophyric texture to clots of quartz crystals was observed (Fig. 4G). The perthitic potassic feldspar (~60 vol%) and quartz (~35 vol%) are the main minerals, whereas plagioclase and biotite are rare. Zircon, magnetite, apatite, fluorite, titanite, and rutile occur as accessory phases, especially filling cavities.

5.1.2. Volcanic rocks

The volcanic rocks occur as centimeter-thick dikes in abrupt contacts with the alkali feldspar granite (Fig. and 4C). There are two varieties: (i) alkali feldspar rhyolite, composed of a brownish aphanitic matrix and phenocrysts of K-feldspar and quartz, occupying about 25 vol% of the rock (Fig. 4H);

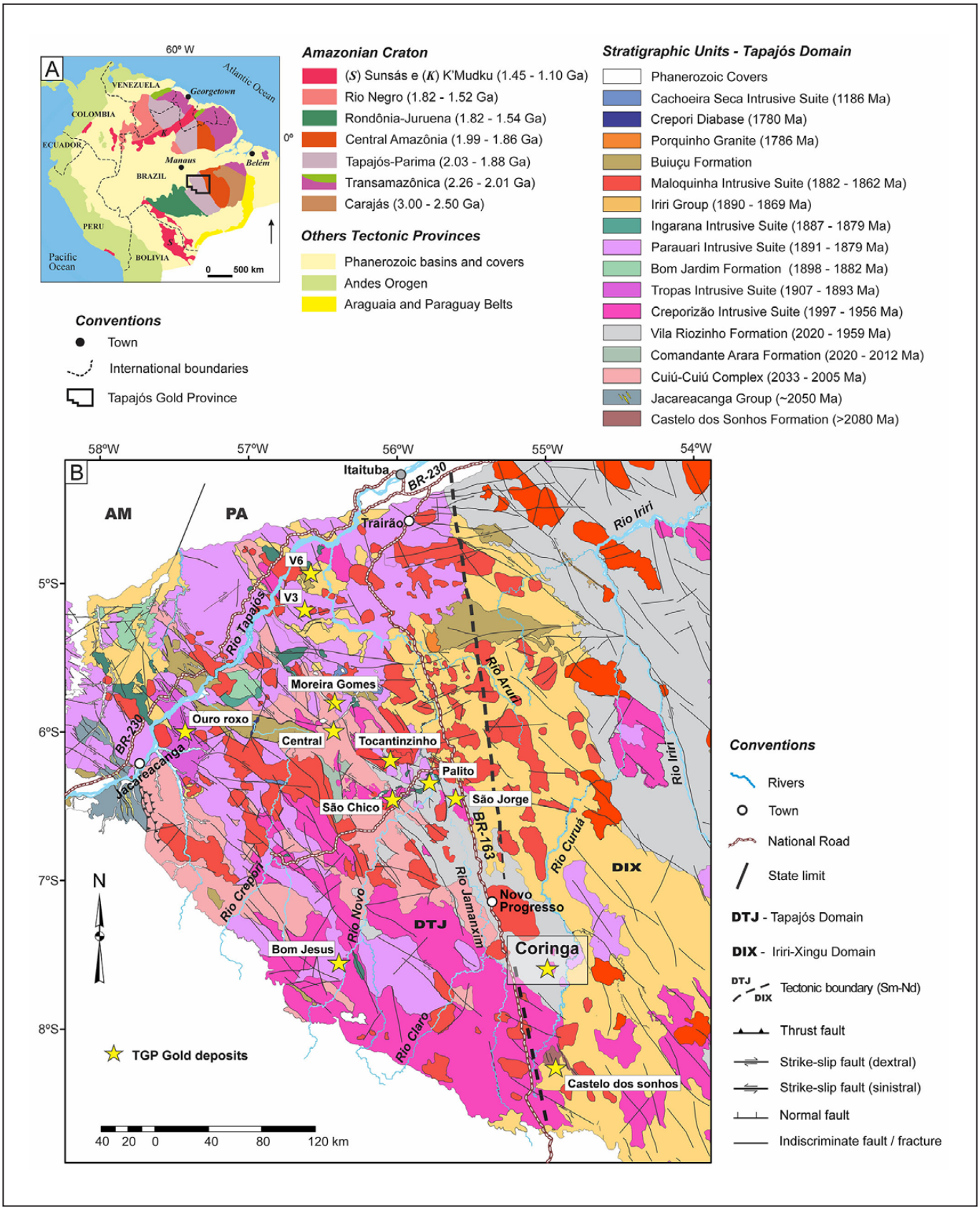

FIGURE 1. A) Geochronological provinces of the Amazonian Craton (Santos et al. 2008) and localization of the Tapajós Mineral Province (TMP); B) Geological map of the Tapajós Domain with localization of some of the main deposits of the TMP. Modified from Vasquez et al. (2014).

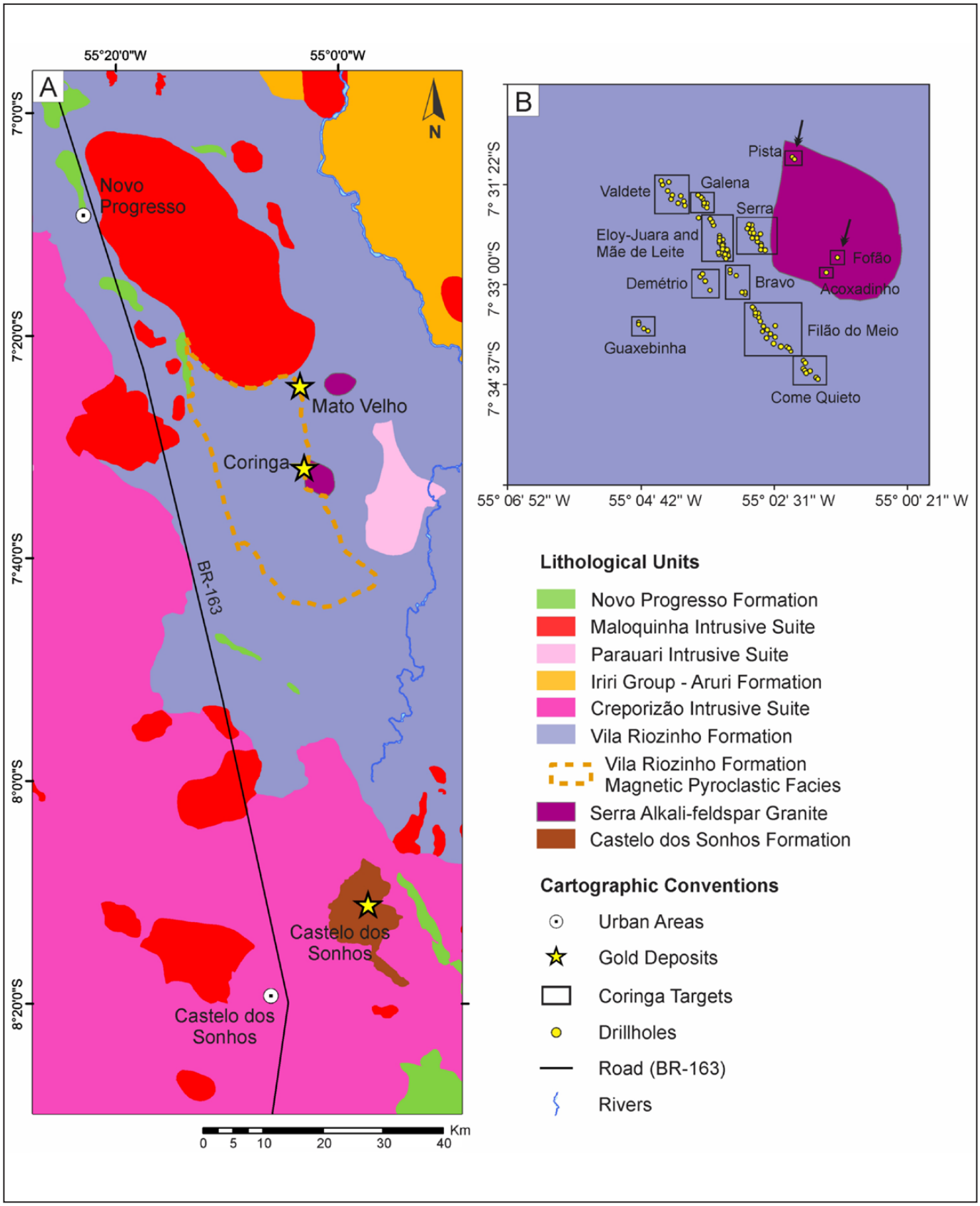

FIGURE 2. A) Geological map of the southeastern TMP and location of the main gold deposits and prospects. B) Geological map of the Coringa deposit with the location of the exploration targets and drill sites. Adapted from Guimarães et al. (2019) and Dzick (2015).

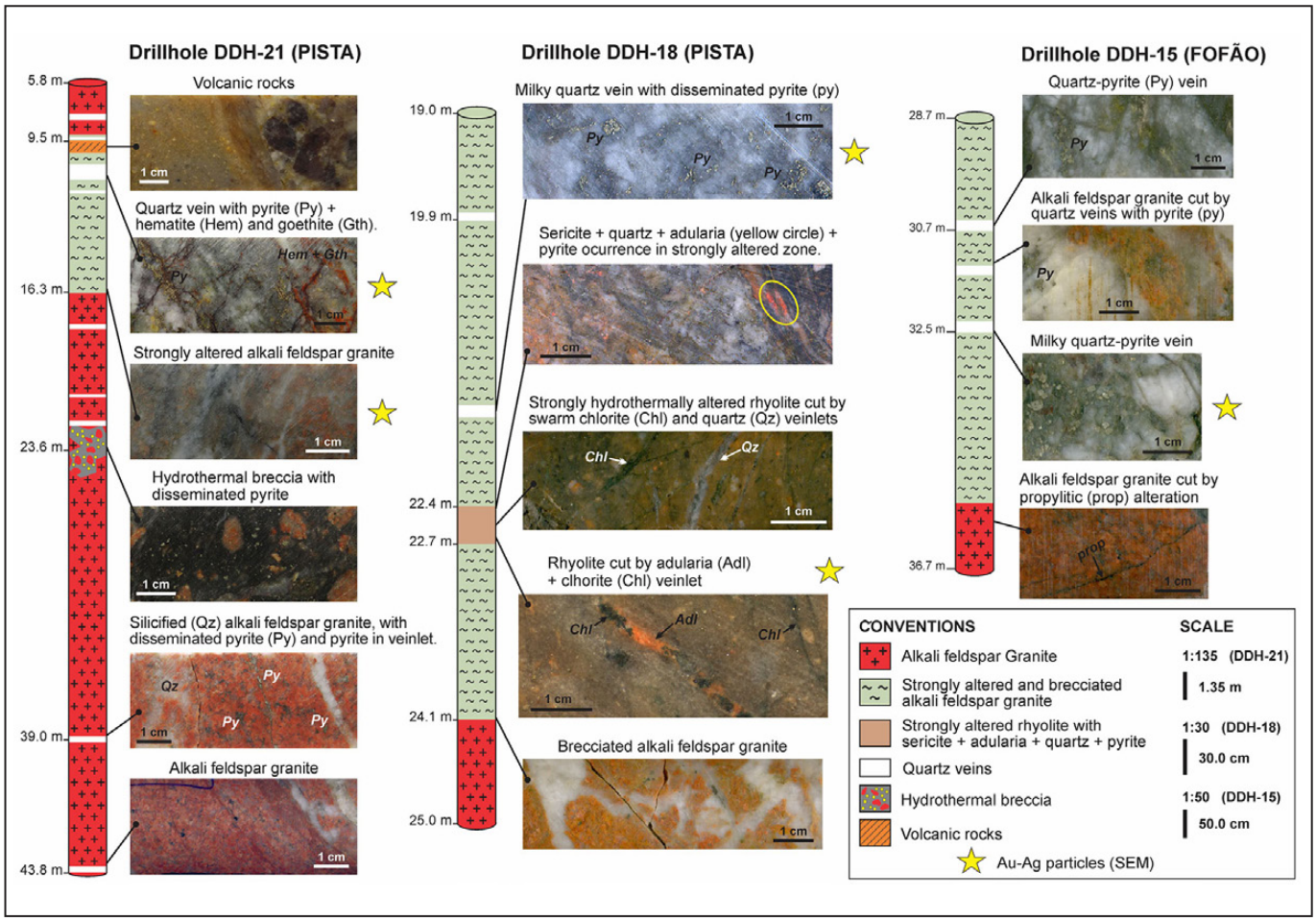

FIGURE 3. Schematic profiles of drill cores from the Pista and Fofão targets showing the host rocks and hydrothermal alteration minerals. (Adl - adularia; Chl - chlorite; Gth - Goethite; Hem - hematite; Py - pyrite; Qz - quartz.).

(ii) lapilli-tuff, formed by a grayish aphanitic matrix, strongly recrystallized with poorly-sorted, sub-angular to sub-rounded clasts, smaller than 3.5 cm (ash to lapilli), as well as pyramidal quartz crystals (Fig. 4I).

5.1.3 Hydrothermal breccias

Hydrothermal breccias are characterized by up to 70 vol% of fine-grained sericite-quartz-rich matrix (Fig. 4D and 4E). Centimetric clasts are mainly composed of angular to sub-rounded alkali feldspar fragments (often altered by sericite and siderite) and show chaotic distribution. Minor quartz and K-feldspar crystal fragments and other lithic fragments (probably volcanoclastic rocks) were observed. Pyrite (up to 5 vol%) is present as dissemination in the matrix and in quartz veinlets crosscutting clasts and matrix (Fig. 4J and 4K). Locally, “vug-like” cavities (up to 1 cm) are present and can be lined by drusy quartz.

5.2. Hydrothermal alteration

The interaction between hydrothermal fluids and host rocks produced different types and styles of hydrothermal alteration that variably modified the mineral assemblage and textures, especially in the alkali feldspar granite. Such hydrothermal alterations may be divided into (i) post-magmatic and pre-mineralization stage, which includes incipient albite and K-feldspar alterations; (ii) syn-mineralization stage, which comprises silicification and quartz veins, sericitization, and carbonatization; and (iii) distal hypogene chlorite – hematite – rutile – epidote alteration zone (Fig. 5). SEM-EDS analyses were carried out on mineralization-related sulfides, carbonate minerals, and chlorite. The most significant results are shown in Table 1.

5.2.1. Albite and K-feldspar alterations

The albite formation is characterized by the replacement of the magmatic feldspars (mainly K-feldspar), starting with the development of abundant perthite to the formation of albite crystals at the rims of the K-feldspars (Fig. 6A), as well as of intergranular crystals and chessboard albite. The potassic alteration is recognized by strong reddish colors and includes K-feldspar-hematite. The post-magmatic K-feldspar replaces the magmatic feldspars (Fig. 6B), whereas hematite replaces the magmatic magnetite (Fig. 6C), including fine impregnations in the magmatic feldspars, especially in the potassic variety. Both types of alterations are selective pervasive and are only observed in the alkali feldspar granite.

5.2.2. Quartz veins and Silica pockets

The most expressive alteration zone in the two targets is marked by the development of quartz pockets and mono- to

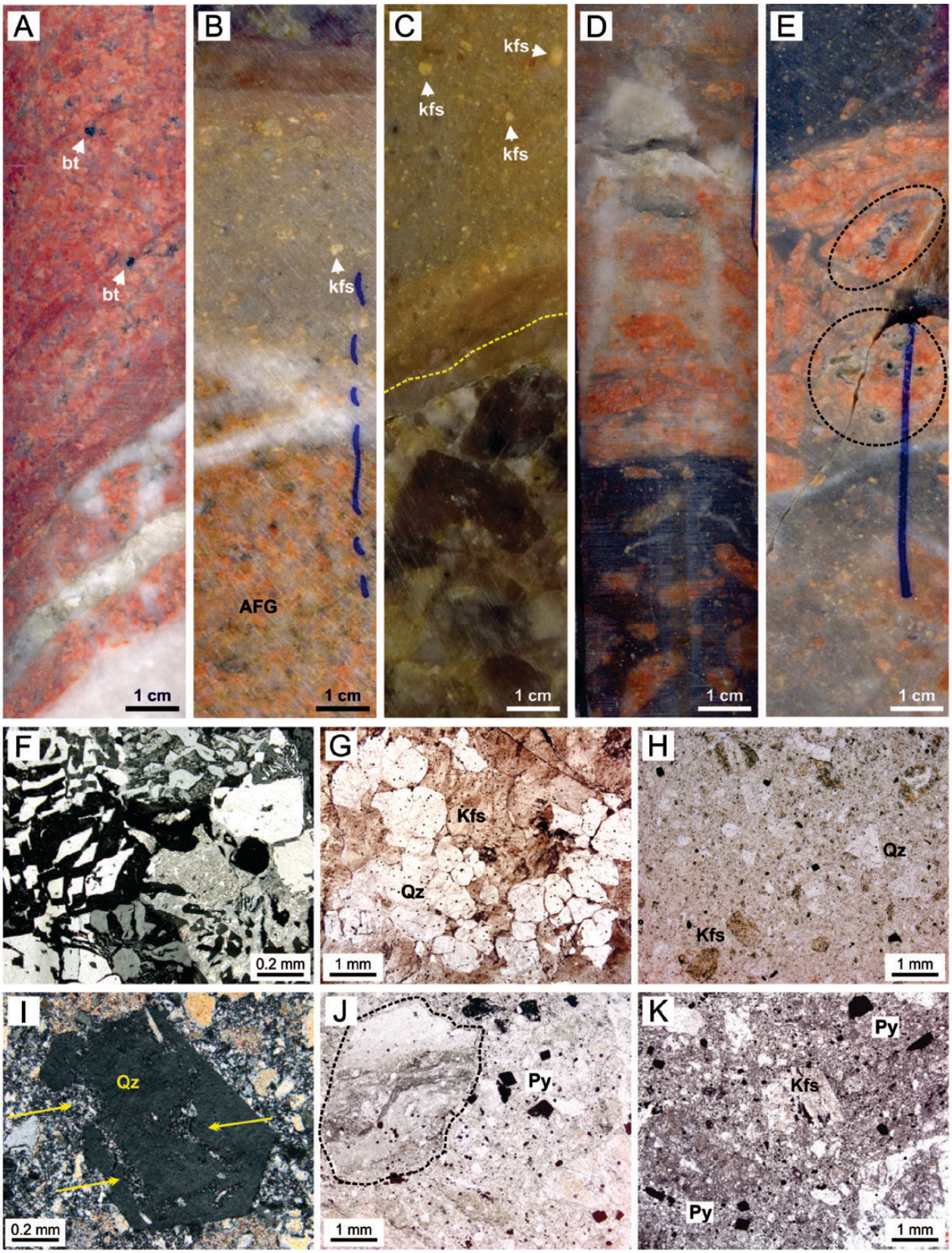

FIGURE 4. Host rocks from the Pista and Fofão targets. A) Hololeucocratic alkali feldspar granite. B) Abrupt contact between alkali feldspar rhyolite and alkali feldspar granite, crosscut by quartz veinlets. C) Contact (dashed line) between alkali feldspar rhyolite and lapilli-tuff. D) Chaotic organization of clasts in hydrothermal breccia crosscut by milky quartz veinlet. E) Millimetric “vugs-like” cavities () in hydrothermal breccia. F) Granophyric texture in the alkali feldspar granite. G) Evolution of the quartz crystallization, resulting in quartz clusters. H) Aphanitic matrix with potassic feldspar and quartz phenocrysts and disseminated pyrite in alkali feldspar rhyolite. I) Euhedral quartz crystal with corroded cores and rims (yellow arrows). J) Lithic fragment (volcanoclastic fragment?) and pyrite dissemination in the breccia matrix. K) Kfs crystal fragment and pyrite dissemination in the breccia matrix. Abbreviations: bt - biotite; kfs – potassic feldspar; qz - quartz; py – pyrite; AFG - alkali feldspar granite.

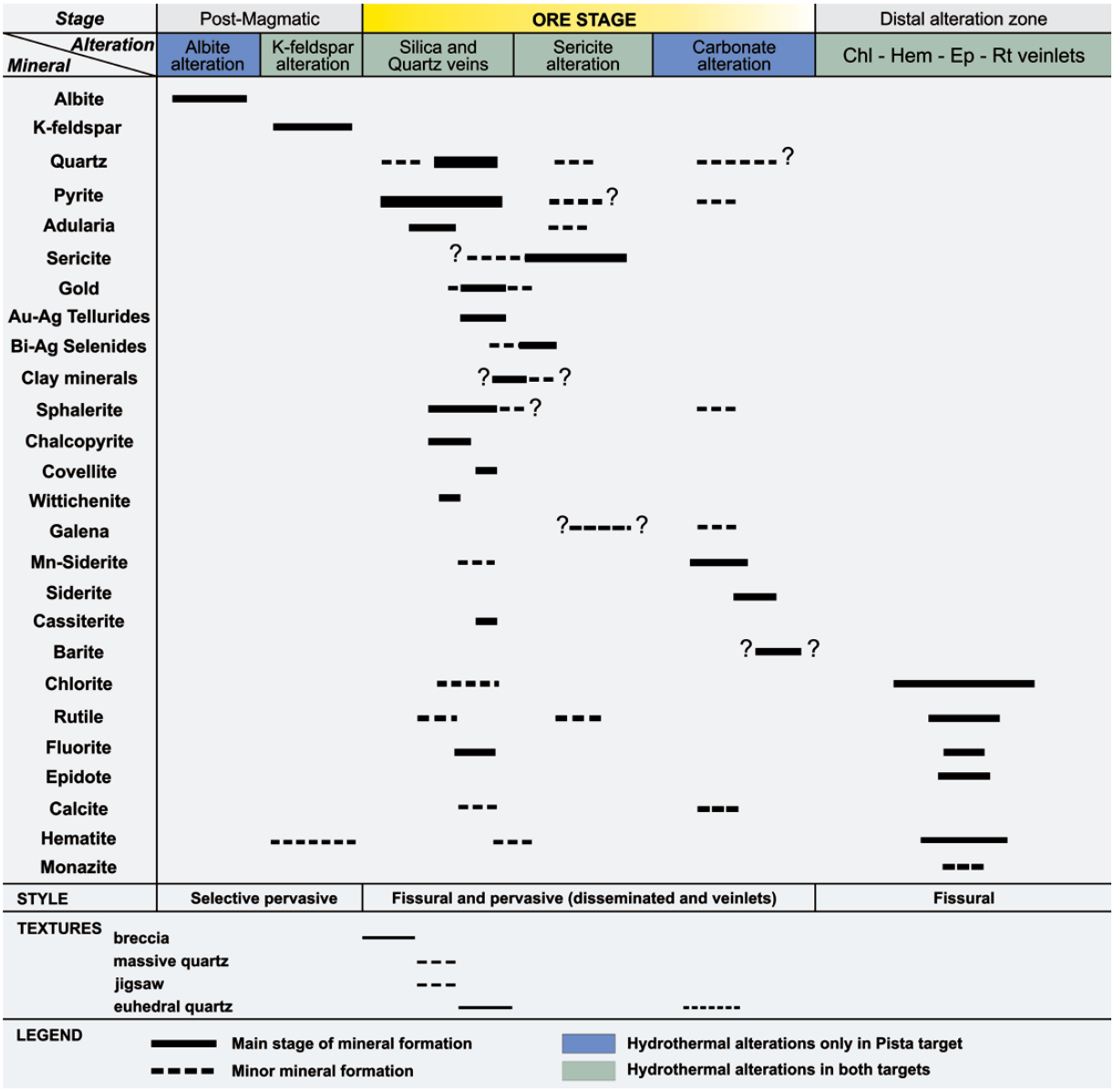

FIGURE 5. Paragenetic sequence of the hypogene hydrothermal alteration in the Pista and Fofão targets.

TABLE 1. Chemical variation (wt.%) of the main hydrothermal phases investigated by SEM-EDS in the Pista and Fofão targets.

Element (wt.%)	Py1	Py2	Sp	Gn	Ccp	Au-Ag Tellurides	Gold	Mn-Sd	Sd	Chl
S	51.45 - 53.24	49.95 - 52.01	29.63 - 32.33	9.74 - 13.10	32.60 - 34.24	*	*	-	-	-
Fe	41.43 - 42.70	40.88 - 42.75	0.22 - 2.96	0.00 - 5.94	27.55 - 28.80	-	-	37.41 - 39.43	45.32 - 53.05	30.27 - 40.29
Zn	0.15 - 0.36	0.17 - 0.45	48.14 - 60.86	0.14 - 0.48	0.09 - 0.21	*	*	-	-	-
Pb	0.87 - 1.66	0.82 - 2.18	0.70 - 2.90	73.22 - 81.35	1.06 - 1.84	*	2.30 - 4.83	-	-	-
Cu	0.09 - 0.22	0.11 - 0.27	0.15 - 9.19	0.16 - 3.89	30.50 - 31.58	*	*	-	-	-
Au	0.46 - 1.13	0.30 - 1.52	1.50 - 5.29	0.18 - 2.29	0.89 - 2.11	6.62 - 20.04	86.89 - 98.10	-	-	-
Ag	0.00 - 0.10	0.00 - 0.26	0.06 - 0.36	0.00 - 0.83	0.05 - 0.13	52.79 - 64.15	*	-	-	-
Te	0.16 - 0.56	0.21 - 0.37	0.18 - 0.55	0.32 - 1.05	0.21 - 0.31	15.79 - 38.03	1.69 - 1.79	-	-	-
Bi	0.74 - 2.31	0.82 - 2.03	1.06 - 3.41	1.76 - 4.22	1.40 - 2.53	*	2.20 - 2.97	-	-	-
Si	-	-	-	-	-	-	-	-	-	12.74 - 14.67
Al	-	-	-	-	-	-	-	-	-	11.04 - 12.28
Mn	-	-	-	-	-	-	-	6.30 - 17.11	0.28 - 1.74	-
Mg	-	-	-	-	-	-	-	0.40 - 1.78	0.87 - 2.43	1.33 - 2.81
C	-	-	-	-	-	-	-	4.68 - 7.20	7.43 - 9.80	-
O	-	-	-	-	-	-	-	31.49 - 38.78	35.86 - 40.53	30.14 - 41.12

Abbreviations – Chl – chlorite; Ccp – chalcopyrite; Gn – galena; Mn-Sd – Mn-siderite; Py1 – pyrite 1; Py2 – pyrite 2;
Sd – siderite; Sp – Sphalerite. – not measured; * values < 0.1%.

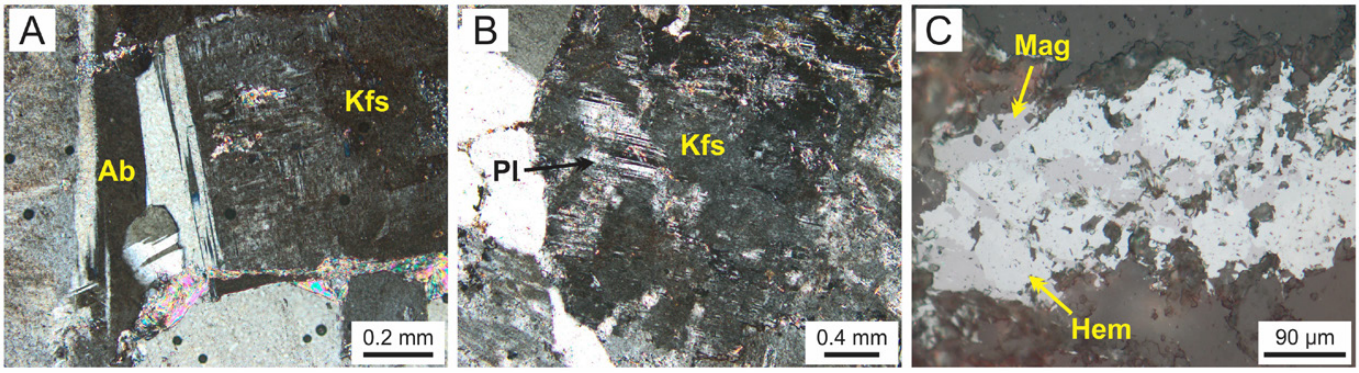

FIGURE 6. Post-magmatic hydrothermal alterations. A) Albite formation at the rims of the K-feldspar. B) Hydrothermal K-feldspar overlapped in plagioclase. C) Orthomagmatic magnetite replaced by hydrothermal hematite. Abbreviations: Ab - albite; Hem - hematite; Kfs - potassic feldspar; Mag - magnetite; Pl – plagioclase.

poly-minerallic quartz veinlets, which is proximal to the gold mineralization zones (Fig. 7A to 7D). In the alkali feldspar granite, strongly silicified zones and several generations of veinlets form a brecciated and stockwork pattern. The pockets are formed by microcrystalline quartz (massive and jigsaw-textured quartz) associated with pyrite aggregates (Fig. 7E). There are two types of veins: (i) open-space filling veins, in which pseudo-hexagonal quartz crystals with pyramidal terminations show growth zones and increase in size towards the center of the vein (zonal quartz texture). These veins appear to be barren or display only minor sulfides and adularia, calcite and siderite (Fig. 7E to 7I); and (ii) usually wide (up to 1 meter) and sulfide-rich milky veins, with subhedral or sub-rounded coarse-grained quartz crystals. In addition, this vein type includes sericite - rutile - hematite - clay minerals - chlorite - Mn-siderite - fluorite - monazite - barite (Fig. 7C and 7D). The temporal relationship between these veinlets remains unclear since no crosscutting features have been observed. Nevertheless, they are located in the same alteration zone.

5.2.3. Sericite alteration

The equilibrium assemblage comprises sericite - rutile - pyrite - quartz - adularia. It is usually more intense near quartz veins, like irregular hydrothermal halos in the granitic rocks (Fig. 7J and 7K). Magmatic feldspars are mainly replaced by sericite in a pervasive style. Sericite - pyrite microveinlets occur cross-cutting K-feldspars crystals (Fig. 7L). Medium to coarse-grained muscovite crystals (Fig. 7M) with fibrous-radial habit and disseminated fine-grained crystals of adularia (Fig. 7C) can be observed in the strongly sericitized alteration zones.

5.2.4. Carbonate alteration

This alteration process was recognized only in the Pista target. Microveinlets of siderite -quartz and calcite microveinlets including pyrite crystals (Fig. 7N) crosscut the brecciated granites and quartz veins. The pervasive style is recorded in the hydrothermal breccia by intense carbonatization of granitic fragments (Fig. 7O and 7P) and also by dissemination of calcite and Mn-siderite in the breccia matrix. SEM-EDS analysis identified Mn-rich siderite crystals (Fig. 7Q), with Mn-contents ranging from 6.30 to 17.11% (Table 1) and containing micro-inclusions of sphalerite and galena.

5.2.5. Chlorite – hematite – rutile – epidote alteration

Chlorite – hematite – rutile – epidote association occurs as distal veinlets from gold-sulfide zones e in both targets. This alteration also includes fluorite, white mica, and monazite (Fig. 8A to 8D). In both targets, the chlorite – fluorite – epidote – hematite assemblage occurs in microveinlets crosscutting K-feldspar alteration zones in alkali feldspar granite. Especially in Pista, chlorite - hematite - rutile assemblage occurs as replacement of adularia, pyrite, calcite and siderite crystals from previous quartz veinlets. (Fig. 8E to 8I).

5.3. Gold-Sulfide assemblage

In the Pista and Fofão targets, the sulfide-gold assemblage is disseminated in the wall-rocks and in veinlets and in the matrix of breccias. In addition to gold and silver, the mineralogical assemblages consist of pyrite and sphalerite, with minor amounts (<1 vol%) of galena and chalcopyrite. Fissure-filling gold mineralization occurs as pyrite-rich quartz veinlets up to 50 cm long. In the Fofão target, the sulfide assemblage is dominated by pyrite, with lesser amounts of sphalerite and galena.

At least three generations of pyrite were recognized: (1) agglomerates of subhedral to euhedral pyrite (py1) in silicified and brecciated zones (Fig. 9A), (2) cubic crystals (py2) in equilibrium with sericitic alteration (Fig. 9B), and (3) cubic crystals (py3) in equilibrium with calcite and siderite in carbonated zones. The sphalerite shows semi-opaque anhedral crystals, partially replaced by galena (Fig. 9C). Chalcopyrite occurs as exsolutions (chalcopyrite disease?) in sphalerite and exhibits anhedral crystals (Fig. 9D). Galena occurs in fracture-fillings and replaces pyrite and sphalerite at their rims. The SEM-EDS analysis (Table 1) shows that sphalerite is the sulfide phase with the higher Au content (inclusions?), varying from 1.50 wt% to 5.29 wt%, and lower Fe content (<2.96 wt%) (Fig. 9E), corresponding to very low % FeS. In addition, in the Fofão Target crystals of wittichenite (Cu_3BiS_3) and covellite (CuS) were recognized (Fig. 9F and 9G). The pyrite crystals show partial replacement by barite and cassiterite in microfractures (Fig. 9H and 9I).

Three styles of gold-silver mineralization were observed at Pista: (i) abundant Ag-Au tellurides included in pyrite (Fig. 10A and 10B), (ii) microparticles (< 5 µm), with >95 wt% Au, spatially with pyrite, sphalerite, and hematite in sulfide-rich

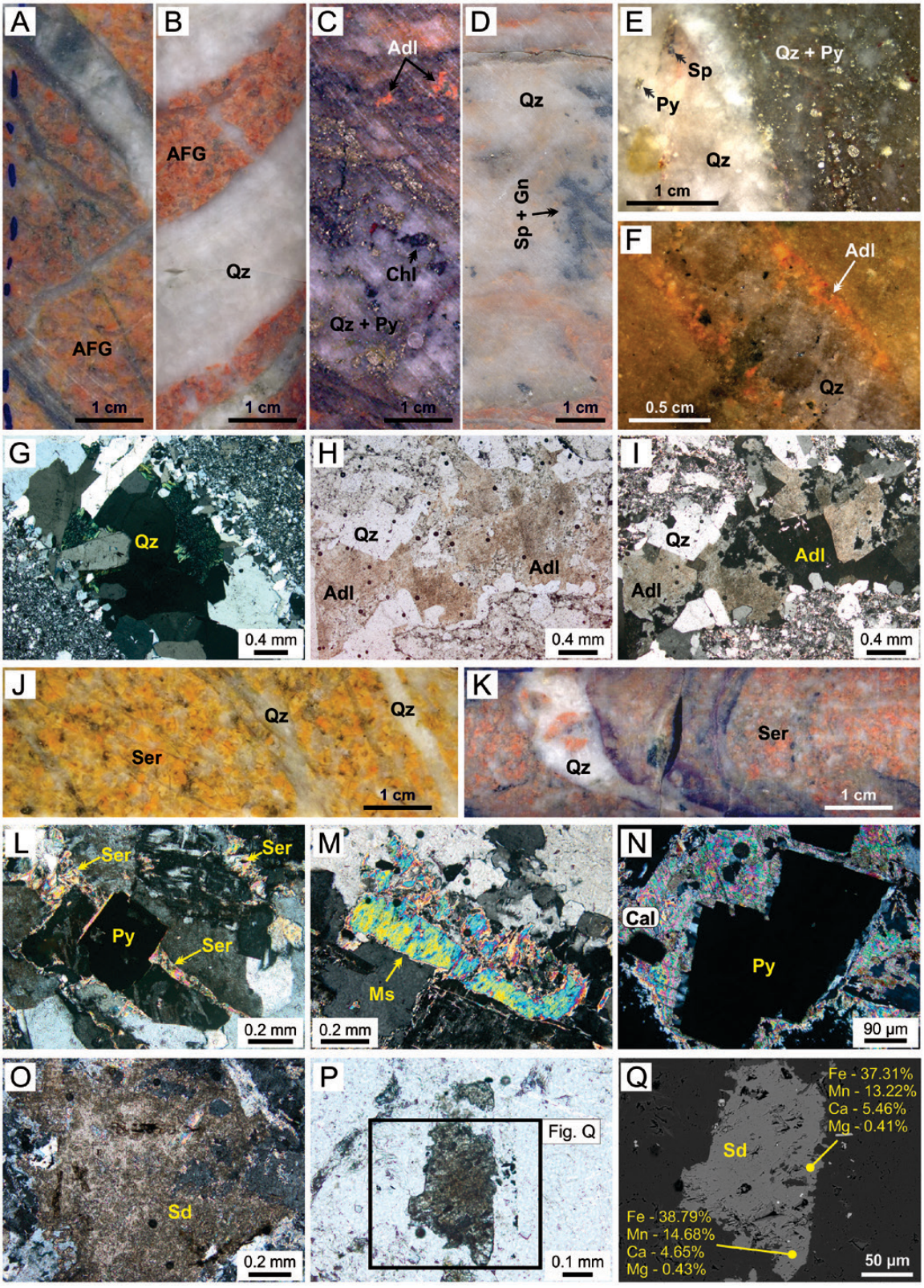

FIGURE 7. Syn-mineralization hydrothermal alteration in the Pista and Fofão targets. A) Two different generations of quartz veinlets crosscutting the alkali feldspar granite. B) Barren, milky quartz vein cross-cutting alkali feldspar granite. C) Silicified zone containing sericite, chlorite and disseminated pyrite and adularia. D) Silicified zone with sphalerite and galena. E) Two main types of quartz veins: milky and anhedral, massive quartz with pyrite aggregates. F) Quartz veinlet with fine-grained adularia crystals at the margin, in contact with alkali feldspar rhyolite wall-rock. G) Pseudo-hexagonal zoned quartz and chlorite in veinlet cross-cutting alkali feldspar rhyolite. H) Micro-cavity filled by euhedral quartz and adularia. Note the pseudo-orthorhombic habit and the pyramidal ends. I) Figure H under crossed nicols. J) and K) Sericite-rich alteration zones in silicified alkali feldspar granite. L) Cubic pyrite in the sericite-rich alteration zone. M) Muscovite in a sericite-rich zone. N) Cubic crystals of pyrite associated with calcite. O) Granitic fragment strongly altered by siderite in the hydrothermal breccia. P) Mn-siderite disseminated in hydrothermal breccia. Q) Chemical composition of Mn-siderite showing Mn contents of 13.22% and 14.68%. Abbreviations: Adl - adularia; Chl - chlorite; Gn - galena; Ms - muscovite; Py - pyrite; Qz - quartz; Ser - Sericite; Sp - sphalerite.

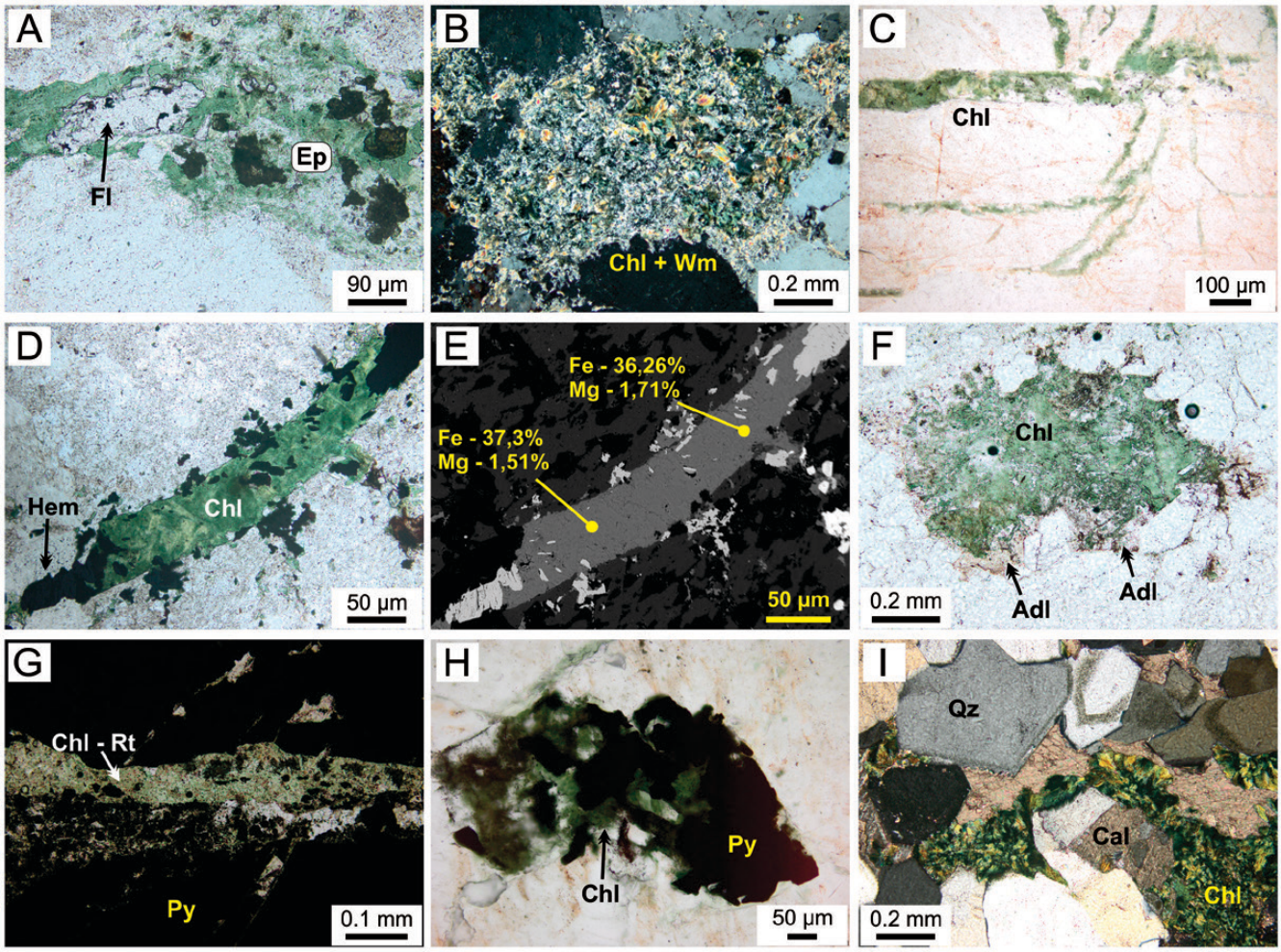

FIGURE 8. Chlorite – hematite – rutile – epidote distal alteration. A) Chlorite veinlet in equilibrium with fluorite and epidote crystals. B) Aggregate of chlorite - white mica in alkali feldspar granite. C) Chlorite microveinlets cross-cutting K-feldspar alteration zone in Fofão target. D) Chlorite - hematite veinlet cross-cutting alkali feldspar granite. E) Backscattered images with EDS analyses from figure E, showing Mg-poor chlorite (Mg <1.71 wt%). F) Late chlorite replacing adularia in quartz veinlet in alkali feldspar rhyolite. G) Late chlorite – rutile veinlet crosscutting pyrite crystal. H) Chlorite replacing pyrite crystal at its rims. I) Chlorite replacing calcite in barren quartz veinlet. Growth zones in euhedral quartz crystal (zonal quartz texture). Abbreviations: Adl - Adularia; Chl - Chlorite; Ep - Epidote; Fl - fluorite; Py - Pyrite; Qz - Quartz; Rt - rutile; WM - White mica.

quartz veinlets (Fig. 10C to 10E), and (iii) 'free' microparticles (< 5 µm) in quartz veins (Fig. 10F). In both targets, Ag is located in hessite (Ag_2Te), Bi-Cd-Te and Bi-Se alloys are located in sericite-rich alteration zones including in pyrite-rich quartz veins (Fig. 10G to 10I).

5.4. Fluid Inclusions

5.4.1. Petrography, types and distribution

Fluid inclusions were observed in quartz crystals from mineralized veinlets of the silicification zone (Fig. 11A). Such crystals are subhedral or sub-rounded, with locally hexagonal shapes. The textural evidence of deformation (i.e. strong undulose extinction, recrystallization, and subgrain development) is incipient.

Based on the composition and number of phases at room temperatures (25 ºC), five types of fluid inclusions have been identified: type 1: monophasic H_2O inclusions (only liquid), the most abundant; type 2: two-phase H_2O inclusions (liquid + vapor); type 3: rare three-phase aqueous inclusions (liquid + vapor + solid); type 4: H_2O-CO_2-NaCl inclusions; and type 5: CO_2 "pure" inclusions. All types occur in intra- and transgranular trails, random clusters, and isolated inclusions. These inclusions have been observed and analyzed following Fluid Inclusions Assemblages (FIA) concept (Goldstein and Reynolds 1994; Chi and Lu 2008), which are inclusions spatially associated and interpreted to be trapped at the same time.

5.4.1.1. H_2O-NaCl fluid inclusions (Types 1, 2 and 3)

Monophasic H_2O inclusions are smaller than 6 µm and occur together with the type 2 inclusions in clusters (Fig. 11B), especially in transgranular trails (FIA B). Two-phase H_2O inclusions (type 2 – the most abundant inclusion type in both targets) occur in clusters, intragranular (FIA A) and transgranular (FIA B) trails. In both trails, the inclusions are smaller than 10 µm and liquid-rich (>80% vol.). Locally, in quartz – adularia – sericite veinlets, a small area in a crystal shows liquid-rich inclusions (80 to 95 vol. % liquid H_2O) coexisting with vapor-rich inclusions (50 to 80 vol. % gas H_2O) (Fig. 11C). Three-phase H_2O inclusions are rare and are located only in veins within the Pista target, especially in sphalerite and galena -rich quartz veinlets. These inclusions are associated with H_2O inclusions (types 1 and 2) and in clusters with types 4 and 5 (Fig. 11D and 11E).

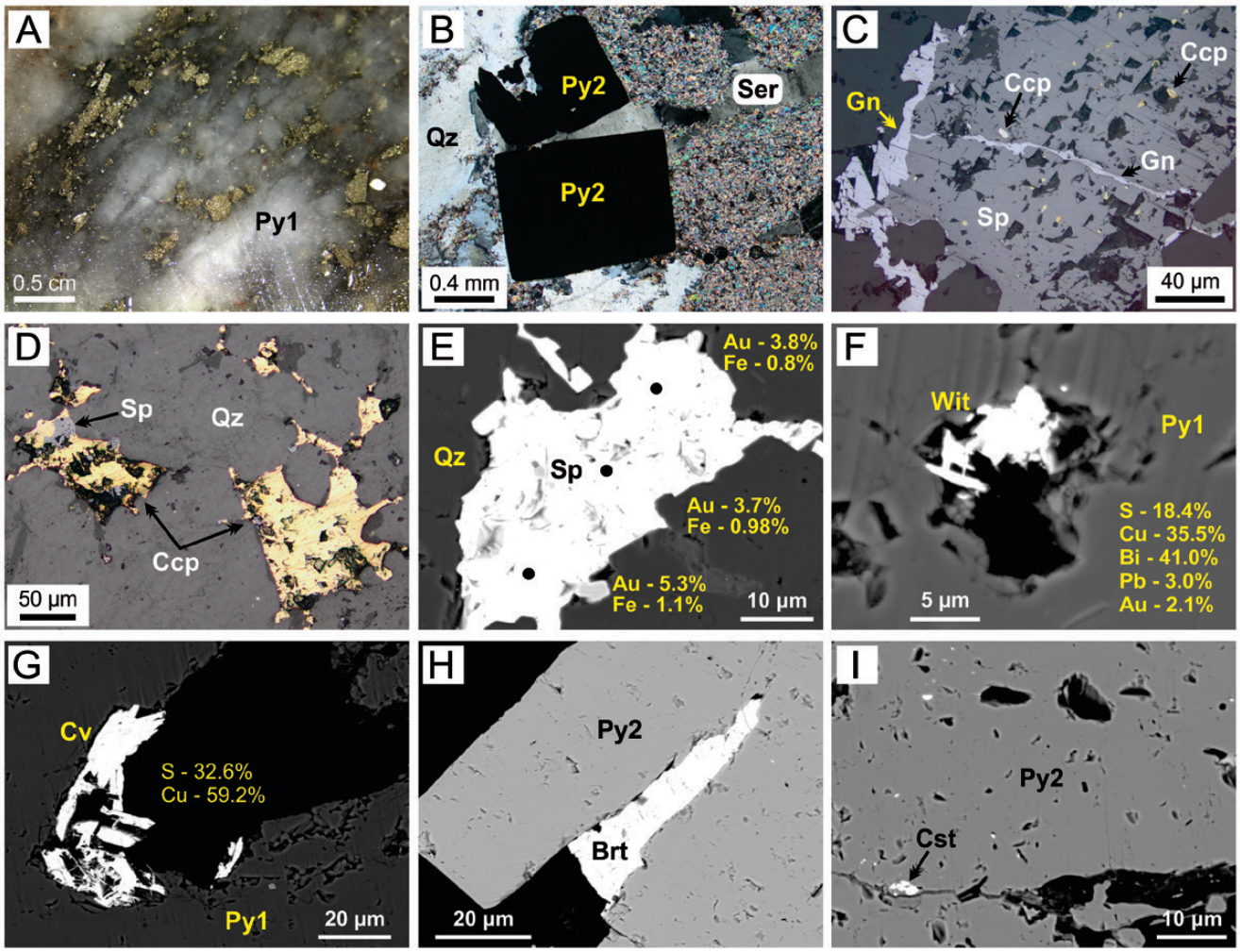

FIGURE 9. Ore textures and equilibrium assemblages in the Pista and Fofão targets. A) Agglomerates of pyrite (py1) crystals in milky quartz veinlet (type 2). B) Euhedral pyrite (py2) crystals in the sericitized zone. C) Anhedral crystal of sphalerite with thin inclusions of chalcopyrite partially replaced by galena. D) Anhedral chalcopyrite with sphalerite in quartz vein (type 2). E) Sphalerite crystals with Au content of 3.7 wt% to 5.3 wt%. F) Wittichenite crystal hosted in quartz vein (type 2). G) Covellite (supergene?) crystal hosted in quartz vein (type 2). H) Cubic crystal of pyrite (py2) partially replaced by barite. I) Cassiterite particle in microfracture of pyrite (py2) crystal. Abbreviations: Brt - barite; Ccp - chalcopyrite; Cst - cassiterite; Cv - covellite; Gn - galena; Py1 - Py2 - pyrite 1 and 2; Qz - quartz; Ser - sericite; Sp - sphalerite; Wit - wittichenite..

5.4.1.2. H_2O - CO_2 - NaCl fluid inclusions (Type 4)

The two- and three-phase H_2O - CO_2 - NaCl inclusions (Figure 11K) are the second most abundant types. In the Fofão Target, they occur in a very few proportions, randomly distributed (clusters), and not associated with aqueous inclusions, whereas, at Pista, they occur in clusters associated with types 2, 3 and 5 (Fig. 11F and 11G) and in isolated clusters (not associated with other inclusions types) (Fig. 11I and 11J). The inclusions show polygonal, sub-rounded and ellipsoidal shapes and range in size from 6 to 18 µm. The carbonic phase occupies between 30% and 60% of the inclusions. In the Pista Target, the volume of the carbonic phase in the richer-CO_2 varieties reaches 90% of the inclusion. Evidence of leakage/necking down is common in inclusions larger than 14 µm.

5.4.1.3. CO_2 pure inclusions (Type 5)

The carbonic inclusions were observed only in the Pista Target, occurring in clusters with types 2, 3 and 4 inclusions and in isolation. The majority of the inclusions are two-phase at room temperature and show polygonal, sub-rounded or ellipsoidal shapes that range in size from 6 to 16 µm (Fig. 11H).

5.4.2. Microthermometric results

We analyzed about 600 inclusions. Inclusions smaller than 4 µm and those with evidence of leakage or necking down were not used in the microthermometric analysis. A summary of the groups and FIA types including the petrographic and microthermometric properties (types and amounts of FIA and IF, melting and partial homogenization temperatures of CO_2, composition, salinity, and temperature of final homogenization) is presented in table 2.

5.4.2.1. H_2O-NaCl inclusions

H_2O-NaCl fluid inclusions in clusters have salinity up to 7.7 wt. % NaCl equiv. (Fofão target) and up to 11.2 wt. % NaCl equiv. (Pista target). These inclusions show final homogenization temperatures between 120 and 275 °C (Fofão target) and 154 to 303 ºC (Pista target) (Figures 12A to 12C). Especially in the Pista target, coexisting vapor- and liquid-rich H_2O-NaCl inclusions show final homogenization temperatures between 290 and 301 ºC, into both to the liquid and vapor state.

Inclusions in pseudosecondary trails (FIA A) and in secondary trails (FIA B) show similar microthermometric

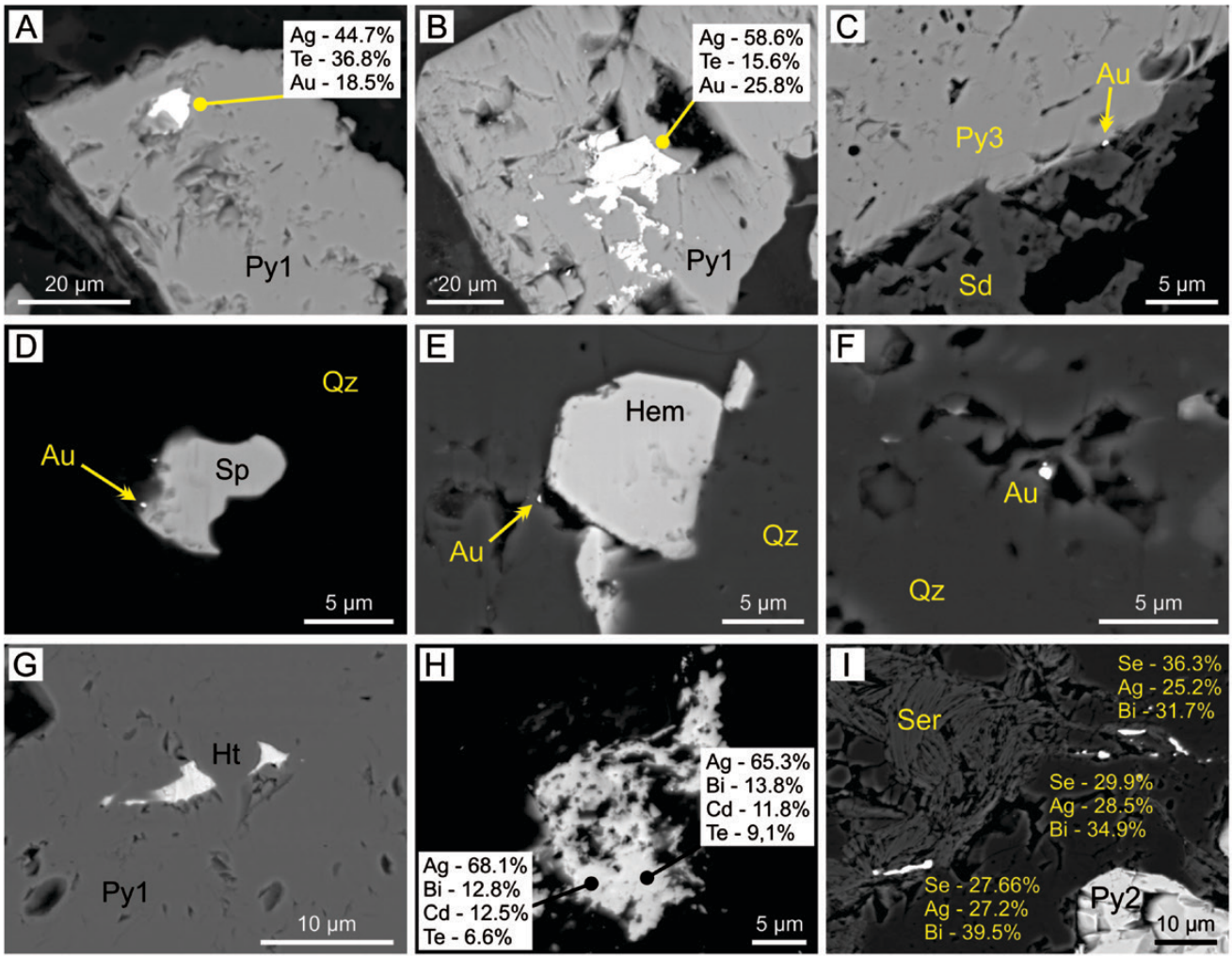

FIGURE 10. Backscattered electron images (SEM) showing the location of Au and Ag in the Pista and Fofão targets. A) Ag-Au tellurides as inclusions in disseminated pyrite (Py1) crystals hosted in rhyolite. B) Ag-Au tellurides as inclusions in pyrite (Py1) of sulfide-rich veinlet hosted in alkali feldspar granite. C) 'Free' gold microparticles at the contact between pyrite (Py3) and siderite. D) Gold microparticle spatially associated with sphalerite in quartz vein. E) Gold inclusion in hematite in sulfide-rich quartz vein (type 2). F) 'Free' gold inclusion in quartz vein. G) Hessite included in pyrite (Py1) hosted in quartz veinlet (type 2). H) Ag-Bi-Cd-Te alloy in pyrite-rich quartz veinlet. I) Ag-Bi selenides associated with sericite crystals. Abbreviations: Hem - hematite; Ht - hessite; Qz - quartz; Py1 - Py2 - Py3 - pyrite 1, 2 and 3; Sd - siderite; Ser - sericite; Sp - sphalerite.

data in both targets (Figures 12D to 12I). The final ice melting occurred between - 4.4 and -0.1ºC (0.0 to 7.0 wt. % NaCl equiv.) and -1.9 to 0.0 º C (0.0-3.2 wt. % NaCl equiv.) and final homogenization temperatures ranged from 150 to 280°C and 113 to 177 ºC, respectively. In all these cases, the homogenization occurred to the liquid state.

A group of ten inclusions in secondary trails (FIA C) show first melting (~eutectic) between -55.1 and -43.9 ºC indicating composition related to the H_2O-NaCl-$CaCl_2$ system (Borisenko 1977). Final ice melting temperatures ranged from -21.1 to -14.0 ºC (17.8 -23.1 wt. % NaCl equiv.). Considering that hydrate (hydrohalite or antarcticite) melting has not been observed, the salinity was estimated at wt.% NaCl equiv. The homogenization occurred to the liquid state in low temperatures (117 to 132ºC).

5.4.2.2. H_2O-CO_2-NaCl, CO_2 and associated H_2O-NaCl inclusions

The melting ($TmCO_2$) and partial homogenization ($ThCO_2$) of the CO_2, and the clathrate dissociation (TmClat) temperatures in the H_2O-CO_2-NaCl inclusions are similar for both targets. The melting of the solid CO_2 phase was recorded between -57.8 and -56.6 ºC in the Pista Target and between -57.0 and -56.6 ºC in the Fofão target (Figure 13A), indicating the CO_2 as the main volatile (Roedder 1984). Clathrate dissociation occurred between 5.1 and 8.5 ºC in the Pista Target and 6.0 to 8.3 °C in the Fofão target, implying a low salinity fluid, 3.0-8.9 and 3.4-7.5 wt % NaCl equiv., respectively (Figure 13B). The partial homogenization of CO_2 occurred in both liquid and gaseous states, between 19.9 and 31.1 °C (Figures 13C-13D).

For the "pure" CO_2 inclusions, the melting of CO_2 occurred between -57.1 and -56.6 ºC (Figure 13E). The homogenization occurred between 22.2 and 31.1 ºC, both to the liquid and gaseous state. (Figure 13F).

H_2O-CO_2-NaCl inclusions in clusters with no association with other types of inclusions (Clusters B and E) show similar behavior in both targets. The salinity ranges from 3.0 to 8.9% and the final homogenization temperature ranges between 264 and 359 ºC. In all cases, the final homogenization occurred to the aqueous (liquid) state (Figures14A to 14C).

In the Pista target, H_2O-CO_2-NaCl inclusions coexisting with H_2O-NaCl and "pure" CO_2 inclusions in clusters (Cluster C) have low salinity (3.0 - 8.8 wt.% NaCl equiv.) and final homogenization between 290 and 370 ºC (to liquid), and 315

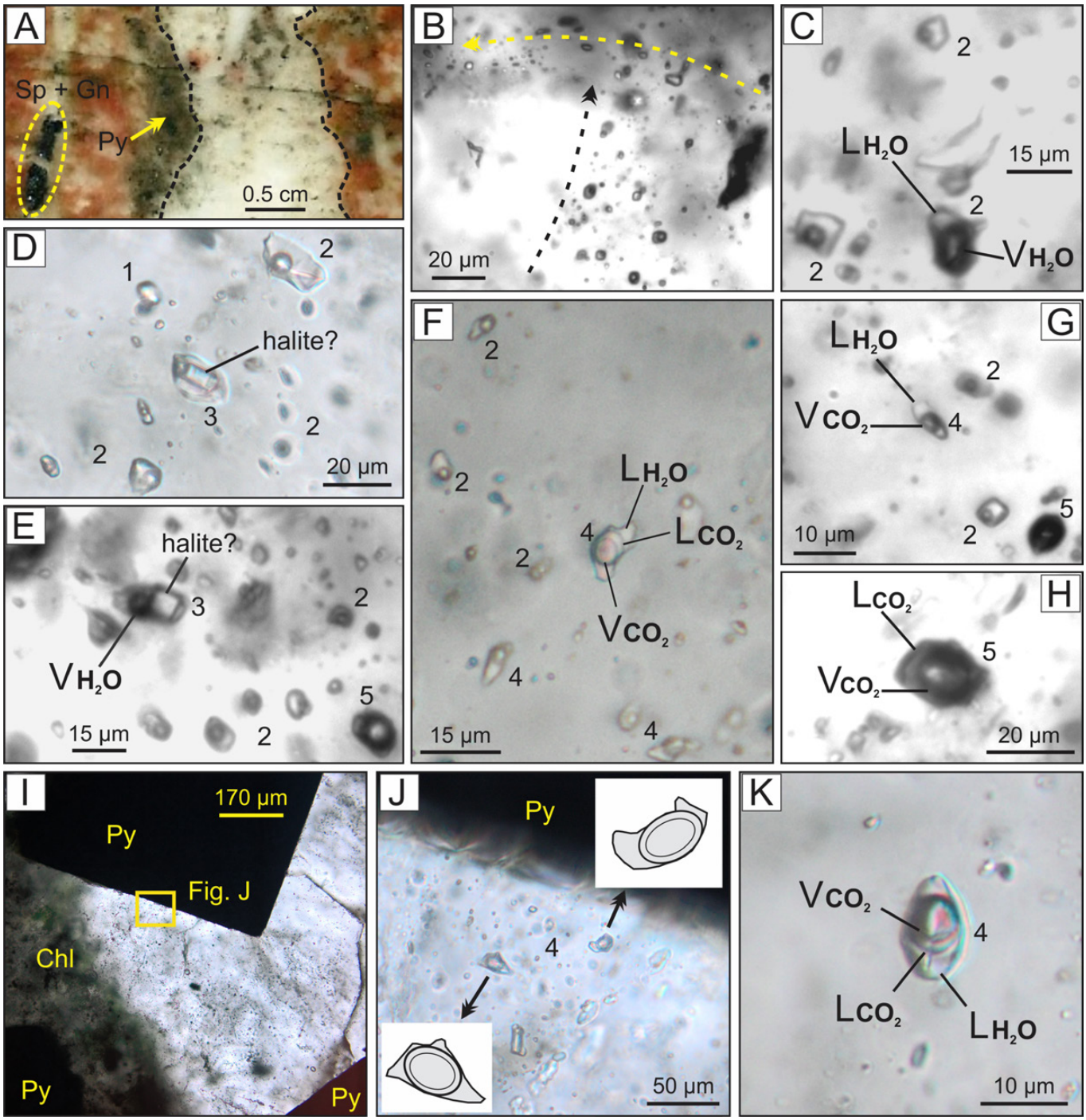

FIGURE 11. Fluid inclusions from the Pista and Fofão targets. A) Doubly polished thin section of sulfide-quartz veinlet hosted in alkali feldspar granite. B) Secondary trail (FIA B, yellow arrow) crosscutting the pseudosecondary trail (FIA A). C) Coexisting liquid- and vapor-rich H_2O - NaCl inclusions. D) and E) Coexisting H_2O - NaCl inclusion containing solid phase (halite?) with H_2O - NaCl inclusions and associated with H_2O - CO_2 - NaCl and carbonic inclusions. F) Coexisting three-phase H_2O - NaCl inclusion with liquid-rich H_2O - NaCl inclusions. G) Liquid-rich H_2O - NaCl, H_2O - CO_2 - NaCl and CO_2 inclusion in pseudosecondary trail. H) Gas-rich CO_2 inclusion. I) Quartz veinlet containing chlorite and cubic pyrite crystals. The yellow area corresponds to the figure J. J) Three-phase H_2O - CO_2 - NaCl inclusions close to pyrite crystal. K) Isolated three-phase H_2O - CO_2 - NaCl inclusion. The numbers in the images indicate the inclusion types. (Chl - chlorite; Py - pyrite; Sp - sphalerite; Gn - galena; LH_2O – liquid water; VH_2O - water vapor; LCO_2 - CO_2 liquid; VCO_2 - CO_2 gas).

TABLE 2. Microthermometric and compositional data of fluid inclusions from the Pista and Fofão targets.

TARGET	MODE OF OCCURRENCE (N)	FI TYPE	X	Tm CO_2 (°C)*	Th CO_2 (°C)* (n)	X CO_2*	X H_2O*	NaCl (%)* (n)	Final Th (°C)* (n)
PISTA	Cluster (27)	1 - 2 - 3	154					0.0 - 11.22 (154)	154 - 303 (112)
	Pseudosecondary Trail - FIA A (10)	2	59					0.0 - 7.18 (59)	150 - 280 (55)
	Secondary Trail - FIA B (9)	1 - 2	40					0.0 - 3.23 (40)	125 - 177 (38)
	Cluster (6)	4	31	-57.6 - -56.6 (29)	19.9 - 31.1 (23)	0.069 - 0.704	0.290 - 0.909	3.0 - 8.93 (31)	275 - 359 (25)
	Cluster (24)	2	91					0.0 - 11.22 (91)	281 - 360 (64)
		4	74	-57.8 - -56.6 (66)	21.3 - 31.1 (61)	0.052 - 0.719	0.257 - 0.934	3.0 - 8.77 (74)	290 - 370 (62)
		5	27	-57.6 - -56.6 (27)	22,2 - 31.1 (27)	58.73 - 174.96			
	Isolated FI	2	9					0.18 - 7.02 (9)	166 - 340 (9)
	Isolated FI	5	2	-57.1 - -57.0	30.1 - 30.8	112.41 - 126.54			
	Secondary Trail - FIA C (3)	2	10	H_2O-NaCl-$CaCl_2$ System (Tm Eutetic = -55,1 to -43,9 °C)				17.79 - 23.11 (10)	117 - 132 (10)
FOFÃO	Cluster (11)	2	44					0.0 - 7.73 (44)	120 - 275 (42)
	Pseudosecondary Trail - FIA A (1)	2	6					0.35 - 2.57 (6)	160 - 197 (5)
	Secondary Trail - FIA B (4)	1 - 2	27					0.35 - 2.07 (27)	113 - 160 (20)
	Cluster (3)	4	12	-57.0 - -56.6 (12)	24.6 - 30.2 (12)	0.069 - 0.408	0.582 - 0.921	3.38 - 7.48 (12)	264 - 322 (12)
	Isolated FI	2	1					0.18 (1)	233 (1)
	Isolated FI	4	2	-57.0 - -56.7 (2)	29.7 - 30.9 (2)	0.120	0.865	5.23 (1)	320 (1)

N - number of groups analyzed; X - number of inclusions; * - Maximum and minimum values for the analyzed inclusions; n - number of measures obtained; FI - fluid inclusion.

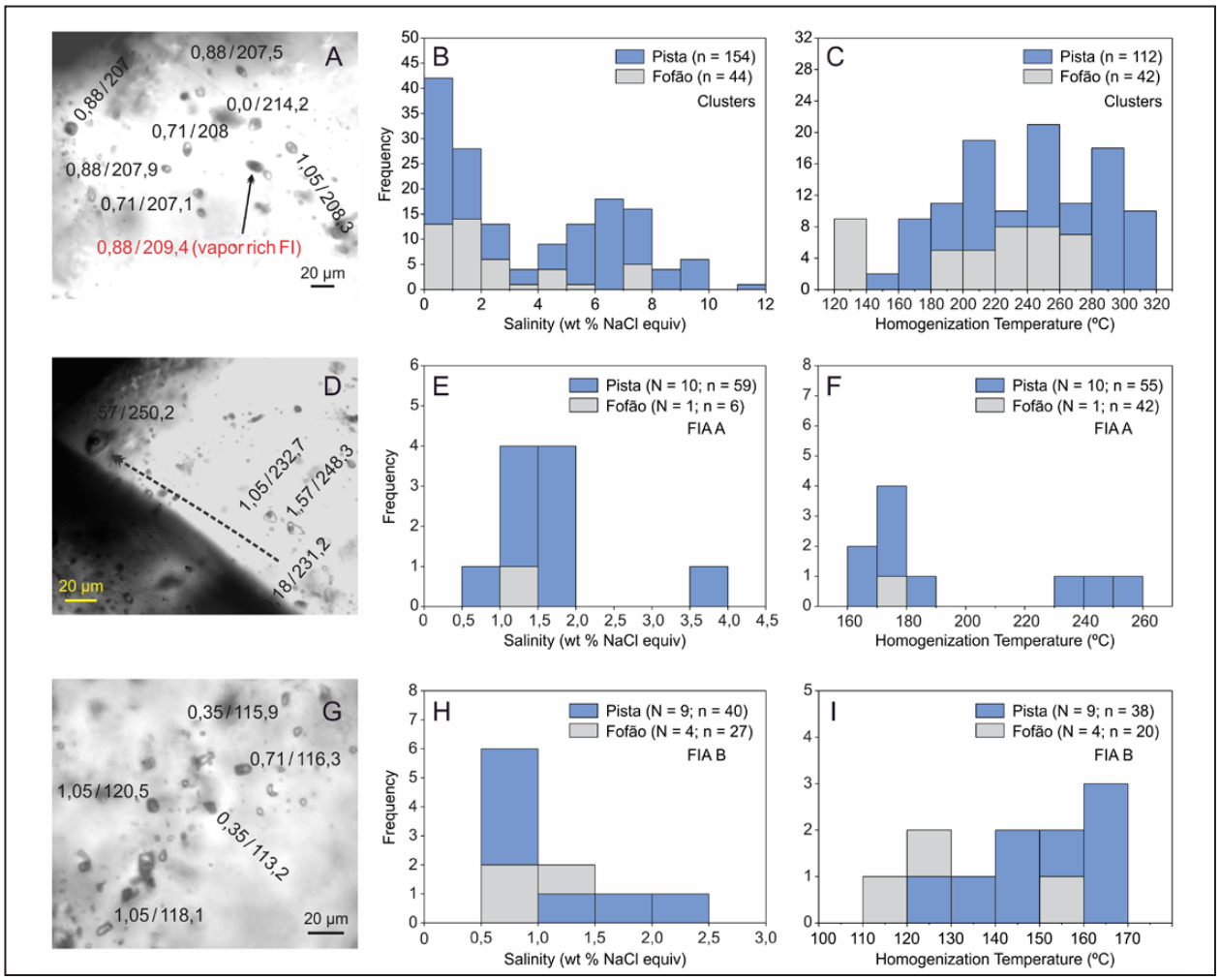

FIGURE 12. Photographs and histograms of salinity and homogenization temperatures for H_2O - NaCl inclusions in clusters (Figures A to C), in pseudosecondary trails (FIA A) (Figures D to F) and in secondary trails (FIA B) (Figures G to I). Note: The histograms for FIA A and FIA B shows the mean values of salinity and temperature for each FIA, (N - Number of FIA analyzed; n - total of inclusions analyzed. The numbers near the inclusions stands for salinity/ homogenization temperature).

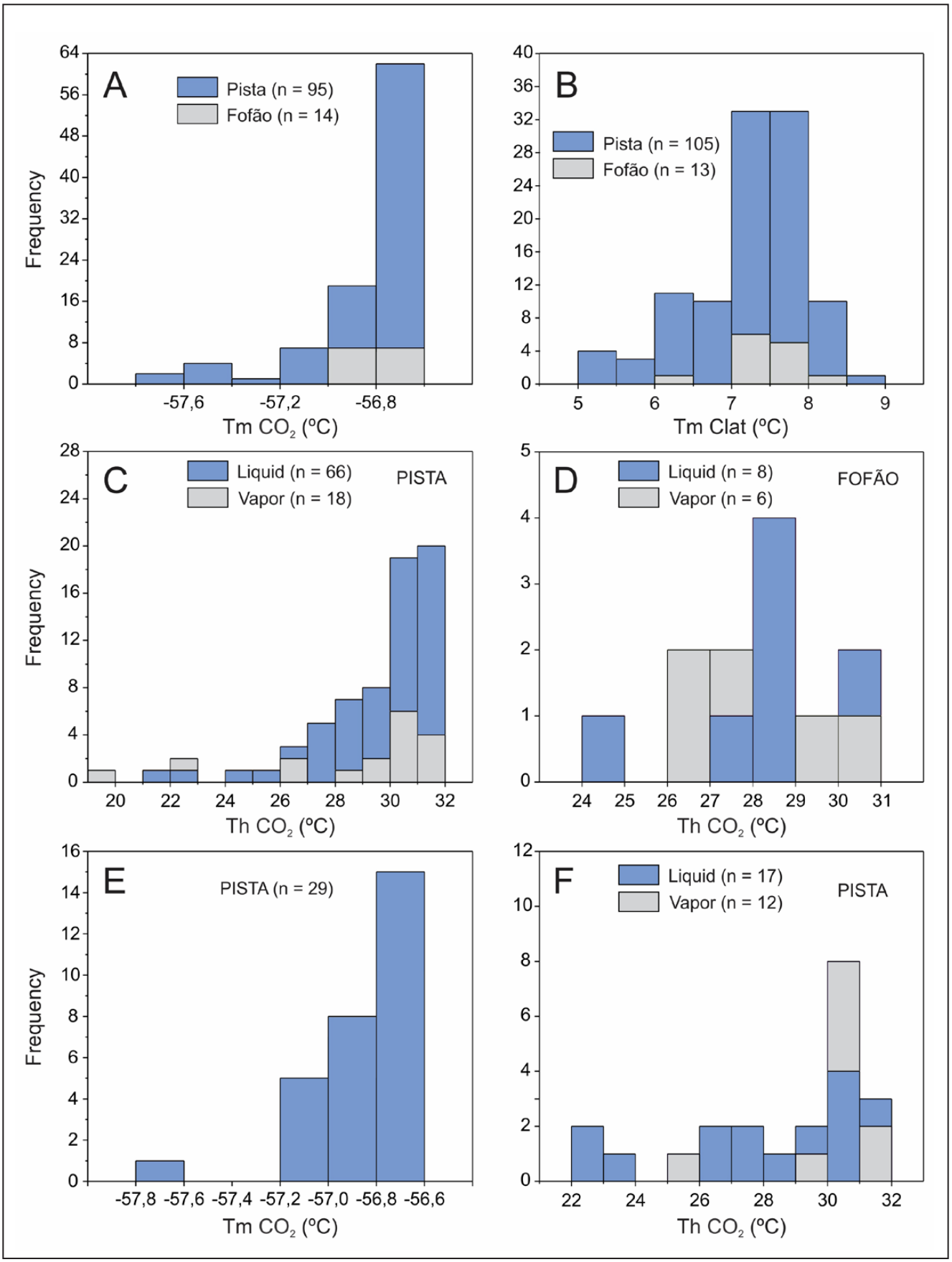

FIGURE 13. Histograms of CO_2 melting ($TmCO_2$) (Figure A), clathrate melting (TmClat) (Figure B), partial homogenization of CO_2 ($ThCO_2$) (Figures C and D) for H_2O-CO_2-NaCl fluid inclusions, CO_2 melting ($TmCO_2$) (Figure E) and the partial homogenization of CO_2 ($ThCO_2$) (Figure F) of carbonic fluid inclusions.

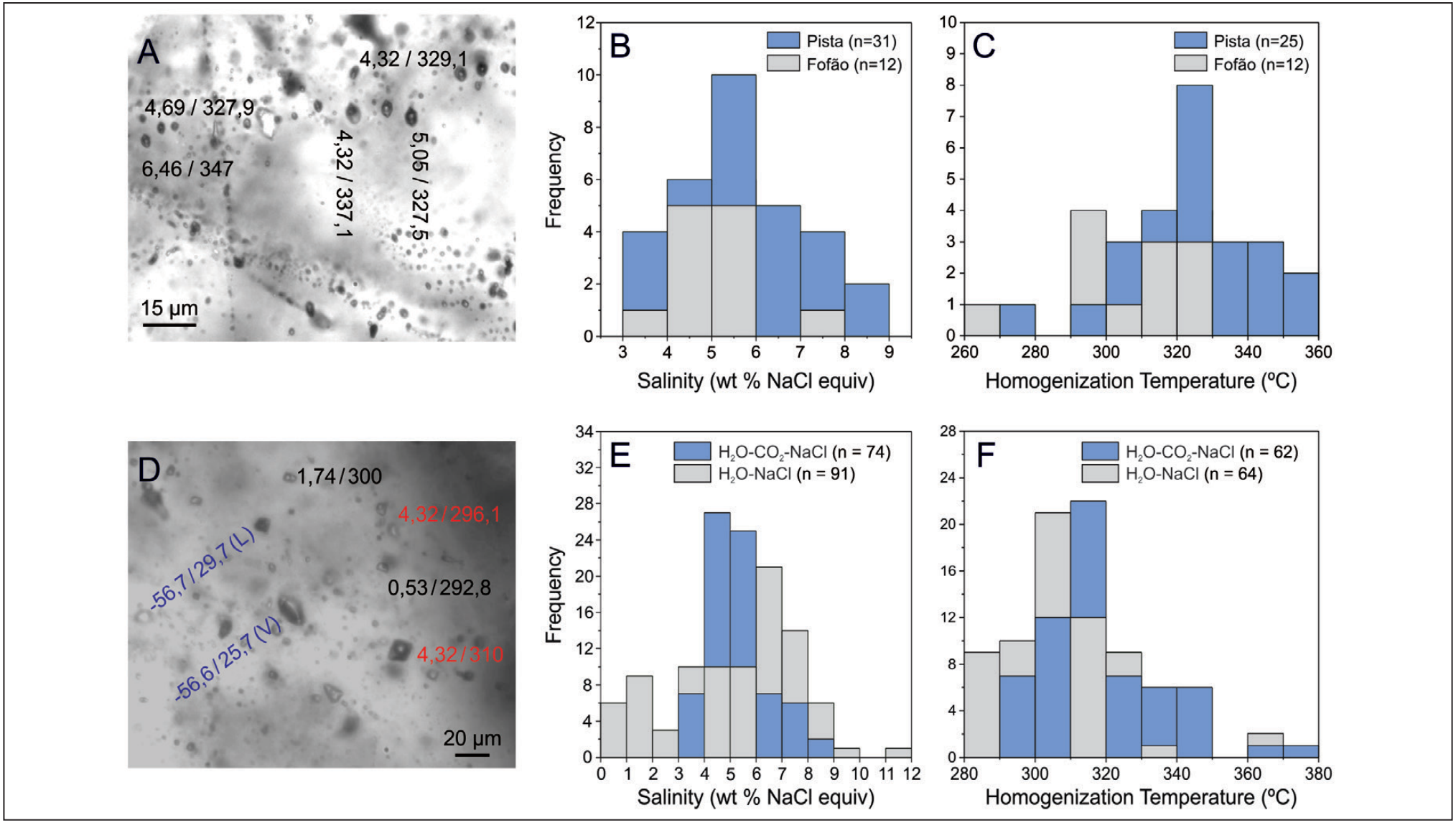

FIGURE 14. A) H_2O-CO_2-NaCl inclusions in polygonal shapes in clusters. B) and C) Histograms of salinity and homogenization temperature for H_2O-CO_2-NaCl inclusions in clusters. D) H_2O-CO_2-NaCl (black numbers), H_2O-NaCl (red numbers) and CO_2 (blue numbers) inclusions in a random association. E) and F) Histograms of salinity and homogenization temperature for H_2O-CO_2-NaCl and H_2O-NaCl inclusions in clusters. (V – vapor; L – liquid; The numbers near the inclusions indicate the final salinity/homogenization temperature for the H_2O-NaCl and H_2O-CO_2-NaCl inclusions and melting/homogenization temperatures of CO_2 for the CO_2 inclusions).

to 370°C (to gas). The coexistent liquid-rich and vapor-rich H_2O-NaCl inclusions have salinity up to 11.2 wt % NaCl equiv. and homogenization temperature between 281 and 360 ºC (in both liquid and gaseous states) (Fig. 14D to 14F).

6. Discussions

6.1. Host Rocks

The main host rock to gold mineralization in the Pista and Fofão targets is a highly-evolved alkali feldspar granite (Serra Granite), which is subordinately associated by abrupt contact with volcanic rocks and hydrothermal breccias. This association, in addition to the presence of miarolitic cavities, granophyric and micrographic textures, indicates emplacement at shallow depth. According to Guimarães et al. (2015), the Serra Granite cross-cuts de volcanic associations, indicating relative late granitic magmatism that can be correlated to granites of the Creporizão Suite, which have high-K and calc-alkaline affinity, post-collisional or continental arc setting characters, including ductile deformed and undeformed rocks as the Old São Jorge (Lamarão et al. 2002).

6.2. Evolution of the paleo-hydrothermal system

The hydrothermal paleosystem that operated in the Pista and Fofão targets generated intense mineralogical and textural modifications in the host rocks. Mineralogical assemblage, textural attributes and temporal relationships for the hydrothermal alterations defined in Pista and Fofão are expressed in table 3.

The sodium and potassic metasomatism are related to the late hydrothermal-magmatic stages. According to Pollard (1983), the albitization of potassic feldspar ($KAlSi_3O_8 + Na^+ \Rightarrow NaAlSi_3O_8 + K^+$) may occur by perthitic exsolution or even by direct replacement at temperatures from 400 to 600 ºC and pressure ≤ 1 kbar. The addition of Na+ and K+ by metasomatism is generally attributed to a residual magmatic fluid at high temperatures (Dilles and Einaudi 1992; Pirajno 1992).

Posteriorly, the paleo-hydrothermal system reached a stage dominated by silica-saturated residual fluids which favored the crystallization of quartz and other hydrothermal phases (sulfides, quartz, sericite, adularia, and carbonates) in open spaces, forming brecciated zones, abundant veins, stockworks and cavities filled by quartz, indicative of crystallization at shallow crustal levels, probably with the participation of meteoric fluid (Barnes 1997; Pirajno 2009), probably recorded in the FIA B and C (Table 2). In this regard, the hydrothermal breccia, present in the Pista target, resulting from hydraulic fracturing, may be interpreted as the earlier and deeper record of hydrothermal activity, close to the granitic intrusion (Serra Granite).

Although described as a late effect, the sericitization is interpreted as an acidic fluid-dominated alteration stage of the host granitic rock in response to the emplacement of quartz veins, causing intense hydrolysis of feldspars in the host rocks. This interpretation may be confirmed by the spatial relationship between these alteration types. In the Pista and Fofão targets, silicified zones (veins and breccias) are associated with irregular sericitic halos in the alkali feldspar granite. These halos imparted greenish and orange colors (alteration of feldspars by sericite) in the granitic rock. During the sericite formation, there was likely the H+ absorption and alkalis liberation to the residual hydrothermal fluid *($3KAlSi_3O_8 + 2H^+ \Rightarrow KAl_3Si_3O_{10}(OH)_2$ - sericite + $2K^+_{(aq.)} + 6SiO_2$),* making this fluid neutral to alkaline pH conditions and contributing for the adularia and quartz crystallization ($K^+_{(aq.)} + Al(OH)^-_{4\ (aq.)} + 3SiO_{2(aq.)} \Rightarrow KAlSi_3O_8$ - adularia + $2H_2O_{(aq.)}$ or $6SiO_{2\ (aq.)} + KAl_3Si_3O_{10}(OH)_2 + 2K^+_{(aq.)} \Rightarrow 3KAl_3Si_3O_8 + 2H^+_{(aq.)}$) (White and Hedenquist 1995; Sillitoe and Hedenquist 2003).

The quartz - adularia - pyrite - sericite assemblage is indicative of mineralization in low-sulfidation epithermal systems (Hedenquist 1987), analogous to the adularia-sericite system described by Hayba et al. (1985). According to Hedenquist et al. (2000), the crystallization of adularia results from boiling fluids, which raises the pH due to CO_2 loss and decreasing salinity with cooling, contributing to the feldspar stability. Hedenquist and Lindqvist (1985) argue that adularia is formed from neutral fluids (pH = 5.5-6.5) between 250º and 350º C. In addition, these conditions must have also contributed to some carbonate precipitation that occurs in quartz veins at Pista and Fofão. The precipitation of carbonate is usually related to neutral to alkaline fluids (a similar condition to that of adularia crystallization) with low salinity and high partial pressure of CO_2 (Barnes 1997; Robb 2006). On the other hand, the hypothesis of carbonate zones results from another fluid pulse cannot be discarded.

In distal portions of the hydrothermal activity, the host rocks (especially the alkali feldspar granite) were affected by cooled aqueous fluids that likely contributed to the formation of the chlorite - hematite - rutile - epidote alteration zones at Pista and Fofão. As described by Reed (1997), this kind of hydrothermal assemblage, similar to propylitic alteration, would be controlled

TABLE 3. Main mineralogical, textural features and temporal relationships of the hydrothermal alterations types observed in Pista and Fofão targets.

ALTERATIONS TYPE	Albite and K-feldspar alteration	Quartz Veins and Silica pockets	Sericite alteration	Carbonate alteration	Chl – Hem – Rt – Ep Alteration
Style	Pervasive	Pervasive and fissural	Pervasive and fissural	Pervasive and fissural	Fissural
Intensity	Moderate	Moderate to Strong	Moderate to Strong	Weak to Moderate	Incipient
Main mineral assemblage	Ab and Kfs - Hem	Qz - Ser - Rt - Sulfides - Adl	Ser - Rt - Py - Qz - Adl	Cal - Sd - Mn-Sd - Py	Chl - Hem - Rt - Ep
Temporal relationships	Post-magmatic alteration. Cross-cut by quartz veins, Cal-Sd and Chl -Hem - Rt - Ep veinlets.	Stockworks and Brecciated zones. Open-space filling polymineralic quartz veins cross-cutting Ab and Kfs alteration zones.	Orange and greenish hydrothermal halos proximal to the (sulfide) quartz veins.	Cal and Sd veinlets cross-cut altered AFG zones and quartz veinlets. Mn-Sd disse-minations in brecciated zones.	Cross-cut K-feldspar alteration zones and gold--sulfide assemblage. Chl - Hem partially replacing Adl, Sd and Cal in quartz veinlets.
Mineralization	Pre- mineralization stage.	Syn-mineralization. Sulfide--rich quartz veins.	Syn-mineralization. Py-rich sericite zones	Syn-mineralization	Distal and post- (?) mineralization zone.

Abbreviations. Ab – Albite; Adl – adularia; AFG – alkali feldspar granite; Cal – calcite; Chl – chlorite; Ep – epidote; Hem – hematite; Kfs – K-feldspar; Py – pyrite; Rt – rutile; Sd – siderite; Mn-Sd – Mn-siderite

by low F/R ratios, therefore host rock controlled. The lack of mafic minerals and plagioclase (usually the most affected) may be the reason for the limited extent of this hydrothermal assemblage at Pista and Fofão. In the main orebodies of the Coringa deposit (Come Quieto, Galena and Mãe de Leite targets), carbonate, chlorite and epidote alteration zones are intense in ignimbrites and marks a distal propylitic halo (Guimarães et al. 2015), similar to what is observed in the Pista and Fofão targets. In addition, based on textural relationships between this association and pyrite crystals (Figure 8F to 8H), chlorite assemblage formation appears to be late in relation to gold-Sulfide assemblage. The replacement of biotite by chlorite can be expressed by the following reaction: *biotite* + $4H^+$ + $6H_2O$ ⇒ *chlorite* + $2K^+$ + $(Mg,Fe)^{2+}$ + $3H_4SiO_4$. The ions released into a residual fluid by the biotite-chlorite reaction must have been consumed by the crystallization of white mica and hematite, which are in equilibrium with chlorite in this zone.

6.3. Hydrothermal fluids evolution and mechanisms of metal precipitation

The fluid inclusion study allowed the recognition of H_2O-NaCl, H_2O-CO_2-NaCl, and CO_2 inclusions. These inclusions occur in spatially associated groups and in isolation, representing the operation of different hydrothermal fluids at different times during the evolution of the paleo-hydrothermal system in the Pista and Fofão targets.

Initially, the aqueous-carbonic and carbonic inclusions with bulk density between 0.252 and 0.936 g/cm3, formed from CO_2-rich aqueous fluid of low salinity (3.0 to 8.9 wt.% NaCl equiv.) and trapped from 370 to 264 °C. The contemporaneous aqueous fluid inclusions of low to moderate salinity (up to 11.2 wt.% NaCl equiv.) are abundant. These inclusions show some criteria that satisfy the immiscibility rules (Ramboz et al. 1982) for this initial stage: (i) the contemporaneous entrapment of different fluid types (i.e., fluid inclusion assemblage of carbonic, aqueous-carbonic and aqueous fluid inclusions); (ii) final homogenization both to the liquid and to vapor states in the same temperature range, (iii) entrapment of fluids with different phase proportions (clusters B and C) and (iv) partitioning of salts into the aqueous-rich phase (Figure 15). Consequently, the pure CO_2 and H_2O inclusions (clusters B, C, and E) could represent the end-members of an H_2O-CO_2-NaCl parental fluid.

Locally, quartz veinlets (with adularia, pyrite - py1 and py_2 - and sericite) host groups of liquid- and vapor-rich H_2O-NaCl inclusions (Fig. 16A-16D), suggesting boiling (Bodnar et al. 1985) between 280 and 370 °C (Fig. 16E). The presence of adularia and hydrothermal breccia are also indicative of boiling in the studied targets (Dong and Morrinson 1995; Jébrak 1997; Hedenquist et al. 2000). Furthermore, these veinlets also contain H_2O-CO_2-NaCl and CO_2 inclusions, indicating, besides H_2O, CO_2 as an important volatile component present in the paleo-fluid system. For this reason, we adopt the "effervescence" term instead of "boiling", as recommended by Wilkinson (2001). The microthermometric data are relatively similar to those obtained by Dreher et al. (1998) for the adularia-rich quartz veins from the Davi and Joel artisanal mines in the central portion of the Tapajós Mineral Province (map on Fig. 1B). According to these authors, the CO_2-poor, aqueous fluids with very low salinity (0.4 and 1.1 wt % NaCl equiv. for Davi and up to 11.2 wt% NaCl equiv. for Joel) were trapped between 220 and 340 ºC.

In the salinity vs. homogenization temperature diagrams (Fig. 17A), a trend of increasing salinity with progressive cooling, common in the effervescence systems (Wilkinson 2001), is not observed, but rather an isothermal trend. As such, the possibility that the part of the hottest aqueous inclusions from clusters A (Pista target) and clusters D (Fofão target) represent an independent H_2O-NaCl fluid (infiltrated meteoric

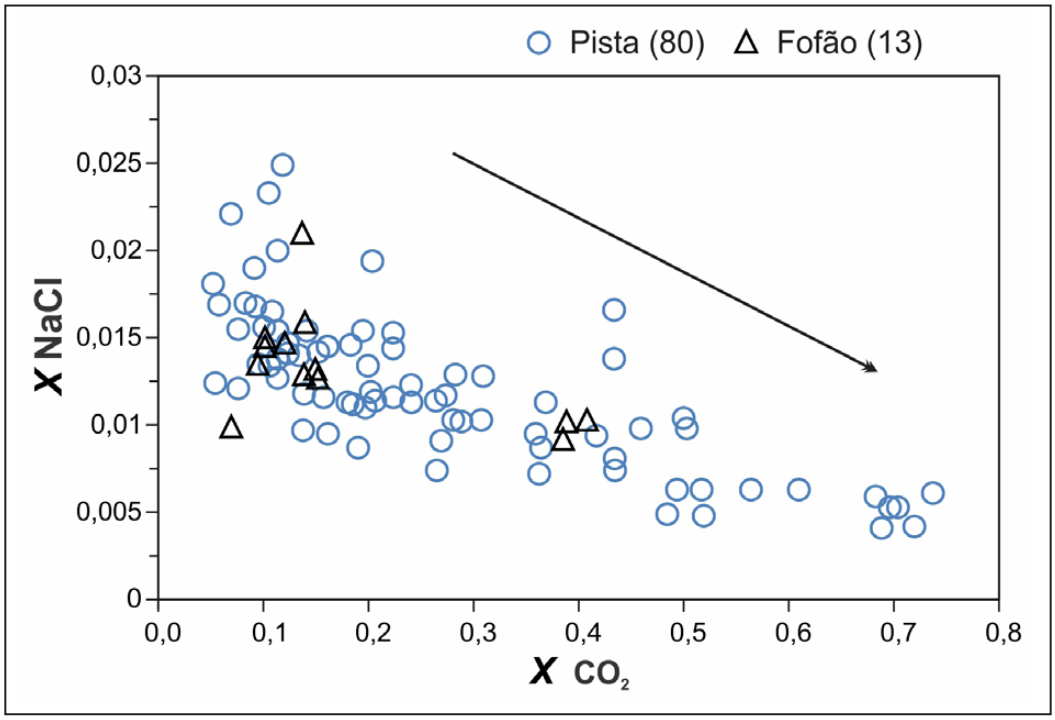

FIGURE 15. XNaCl vs. XCO_2 diagram. The arrow indicates a trend of NaCl molar fraction decreasing with increasing CO_2 molar fraction, suggesting fluid immiscibility. The number in parenthesis represents the amount of inclusions analyzed.

fluids that were heated?), which was isothermally mixed with a hotter fluid (magmatic-origin) is proposed. In the Fofão target, the trends for the initial fluid activities (clusters E and hottest aqueous fluid from clusters D) are not so clear perhaps due to the small number (n=92) of analyzed inclusions (*trend* 1; Fig.17B). It is noteworthy that the aqueous-carbonic inclusions are CO_2-poorer (≤ 0.41 mole %) and late (≤ 323 °C) in the Fofão than in the Pista Target (≤ 0.74 mole %; ≤ 370 °C). Accordingly, the lack of carbonic inclusions may be another indicator of late fluid inclusion trapping in this target.

Secondary liquid-rich aqueous inclusions (FIA B) represent a low salinity fluid (up to 3.2 wt.% NaCl equiv.) with lower temperature (177 to 113 °C), likely more oxidized (suggested by the crystallization of hematite and barite an the end of the hydrothermal activity), that was predominant in a stage of progressive dilution with cooling (Fig. 17A and 17B).

Secondary inclusions of the H_2O-$CaCl_2$-NaCl system (FIA C) suggest that high-salinity fluids must have circulated at later stages (Th = 117 - 123 ºC) of the hydrothermal paleosystem. However, the role and evolution of these fluids is still unknown and further studies about such fluids are necessary.

In magmatic-hydrothermal deposits, boiling and effervescence are important processes for ore precipitation (Skinner 1997). Fluids in low-sulfidation epithermal systems have pH close to the neutral state, are moderately reduced, contain significant H_2S and low CO_2 contents (Reed 1997). The increase in pH during boiling, due to the loss of H^+, H_2S, and CO_2, causes a decrease in the precious and base metals solubility and contribute to its precipitation of precious (Au-Ag) and base metals and also adularia (Simmons et al. 2005; Saunders et al. 2014). Nevertheless, our petrographic data suggest that Au and Ag and base metals precipitation (Zn, Pb, and Cu) are not directly related to the presence of adularia (not cogenetic) and breccias, considering that free-gold, Au-Ag telluride and base metal sulfides occur in the later stages. So, boiling can be interpreted as responsible only for precipitation of the adularia and formation of (non-auriferous) pyrite-rich hydrothermal breccias, with restricted participation in the genesis of the gold mineralization at Pista and Fofão. Another point that reinforces the hypothesis of restricted boiling (in Pista

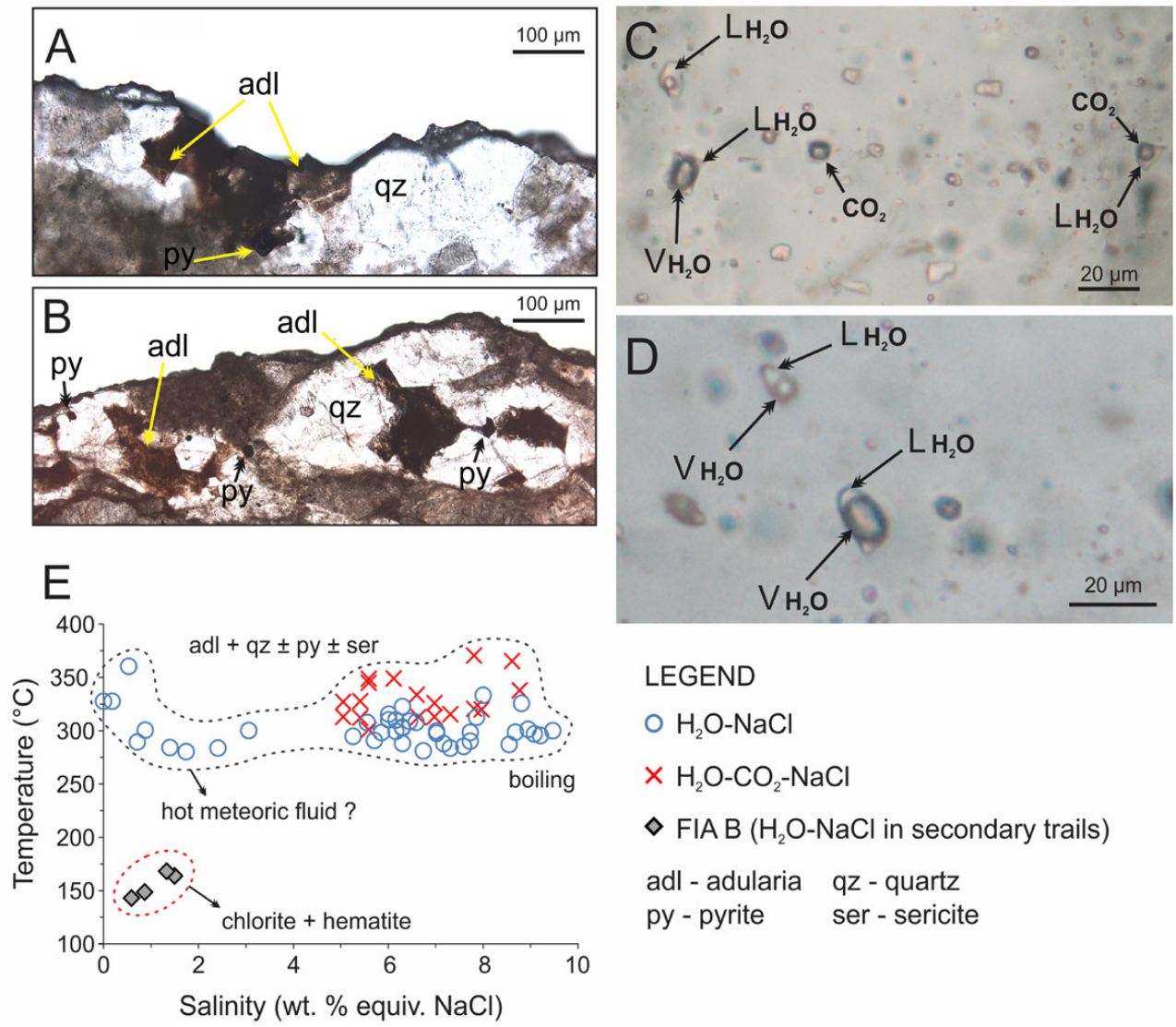

FIGURE 16. Fluid inclusions and physico-chemical data from the adularia crystallization. A) and B) Portions of doubly-polished sections with quartz - adularia - pyrite veinlets. C) Vapor- and liquid-rich H_2O-NaCl inclusions associated with H_2O-CO_2-NaCl and CO_2 inclusions (Cluster C). D) Evidence of boiling conditions by the coexistence of vapor- and liquid-rich aqueous inclusions (Cluster A). E) Salinity vs homogenization temperature diagram with inclusion groups representative of adularia + quartz ± pyrite ± sericite crystallization. (LH_2O – liquid water; VH_2O – vapor water).

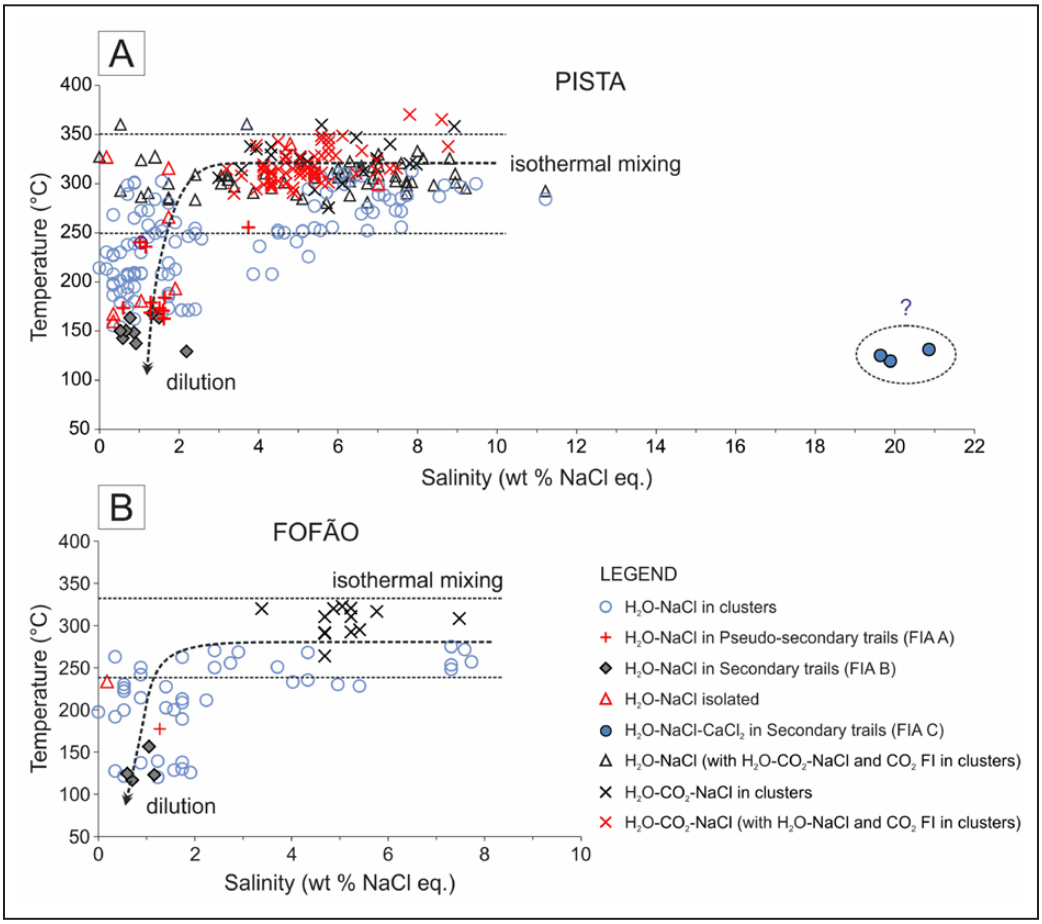

FIGURE 17. Salinity vs homogenization temperature diagram for the Pista (A) and Fofão (B) targets, showing the possible trends and processes responsible for the evolution of the paleo-hydrothermal fluids.

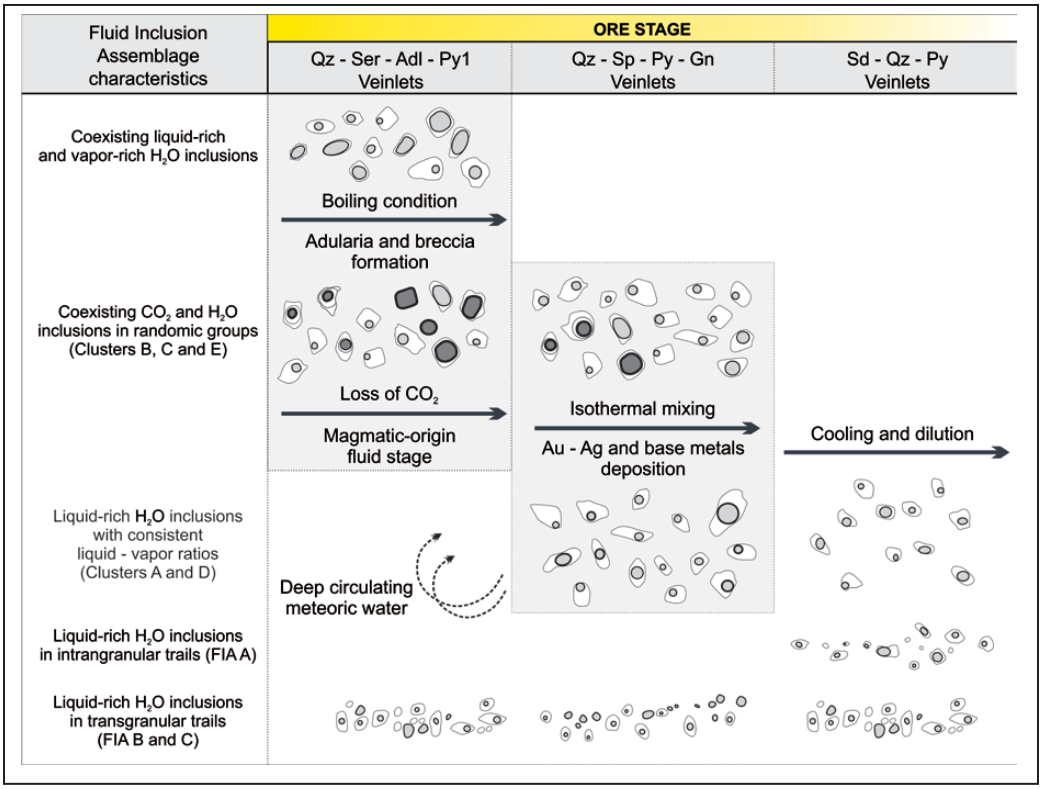

FIGURE 18. Schematic evolution of paleo-hydrothermal fluids in Pista and Fofão targets based on fluid inclusions and microthermometric data.

and Fofão) is the lack of some typical textural of this process (e.g., Moncada et al. 2012), such as: (i) colloform and crustiform textures, (ii) plumose/feathery/flamboyant quartz, (iii) lattice-bladed calcite and (iv) lattice-bladed calcite replaced by quartz. Therefore, based on petrographic and fluid inclusions data, it is possible that Au, Ag, Zn, Pb, and Cu deposition is related to a post-boiling stage of the paleo-hydrothermal system, in which isothermal mixing and subsequent dilution are the main responsible processes for metals deposition (Fig. 18).

Fluid mixing and dilution are important mechanisms for the precipitation of precious and base metals in hydrothermal deposits (Sheppard et al. 1971; Leach and Corbett, 2008). According to Simmons et al. (2005), stable isotope data indicate that mineralizing fluids of epithermal deposits associated with quartz ± calcite ± adularia ± illite containing Au-Ag or polymetallic ores contain a significant amount of meteoric water. In the Creede mining district (Colorado, USA), precious metals ore stages are not related to boiling (Heald et al. 1987). Based on fluid inclusion and stable isotope studies, Hayba (1997) considered fluid mixing processes of magmatic and meteoric fluids as the main process for ore precipitation in the Creede district. At least for the two targets studied here, this interpretation appears to be similar. In addition to the data presented here, in the Galena, Meio, and Serra targets (Figure 2B), quartz crystals from sulfide-rich quartz veinlets yielded variable $\delta^{18}O$ values (7.9 to 15.8‰) (Guimarães et al. 2015), which lead these authors to interpret as a result of variation in temperature during the precipitation, or quartz precipitation in equilibrium with fluids of distinct compositions (magmatic and meteoric?). Therefore, if available fluid inclusions in sulfides and additional isotopic studies (O and H in hydrothermal silicates) are needed for providing further evidence of our hypothesis.

Adopting the hypothesis of mixing and dilution, it is possible that gold precipitation occurred as a result of $Au(HS)^{2-}$ destabilization via mixing of a magmatic fluid with meteoric water [$Au(HS)_2^- + 8H_2O_{(l)} \leftrightarrow Au(s) + 2SO_4^{2-} + 3H^+ + 7.5H_{2(aq)}$] (Cooke and Simmons 2000), which releases H^+ and SO_4^{2-} to the system, making it more acid and oxidized, and contributing for the crystallization of late quartz, hematite, and barite, common phases in the gangue assemblage of Pista and Fofão. On the other hand, CO_2-rich fluids may have contributed to the formation of a telluride-rich ore in the Pista and Fofão targets, as in other low sulfidation epithermal deposits (Saunders et al. 2014).

6.4. Pressure and depth of gold and metals deposition

Considering effervescence as the main process that produced the H_2O-CO_2-NaCl, CO_2 and part of coeval H_2O-NaCl fluid inclusions (clusters B, C, and E) at Pista and Fofão targets, the pressure range was estimated using isochores calculated by the Flincor software (Brown 1989) with the equations of Brown and Lamb (1989) for H_2O-NaCl and Bowers and Helgeson (1983) for the H_2O-CO_2-NaCl fluid inclusions.

The intersections of the isochores of H_2O-CO_2-NaCl fluid inclusions of the minimum (0.36 g/cm³ - Pista and 0.68 g/cm³ - Fofão) and maximum (0.94 g/cm³ - Pista and 0.91 g/cm³ - Fofão) densities with the H_2O-NaCl solvus determined by Bowers and Helgeson (1983) provides pressure and depth trapping conditions of about 0.5-1.7 kbars that correspond to1.4 to 4.7 km depth if a lithostatic pressure gradient is assumed. Particularly at Pista, the intersection between the

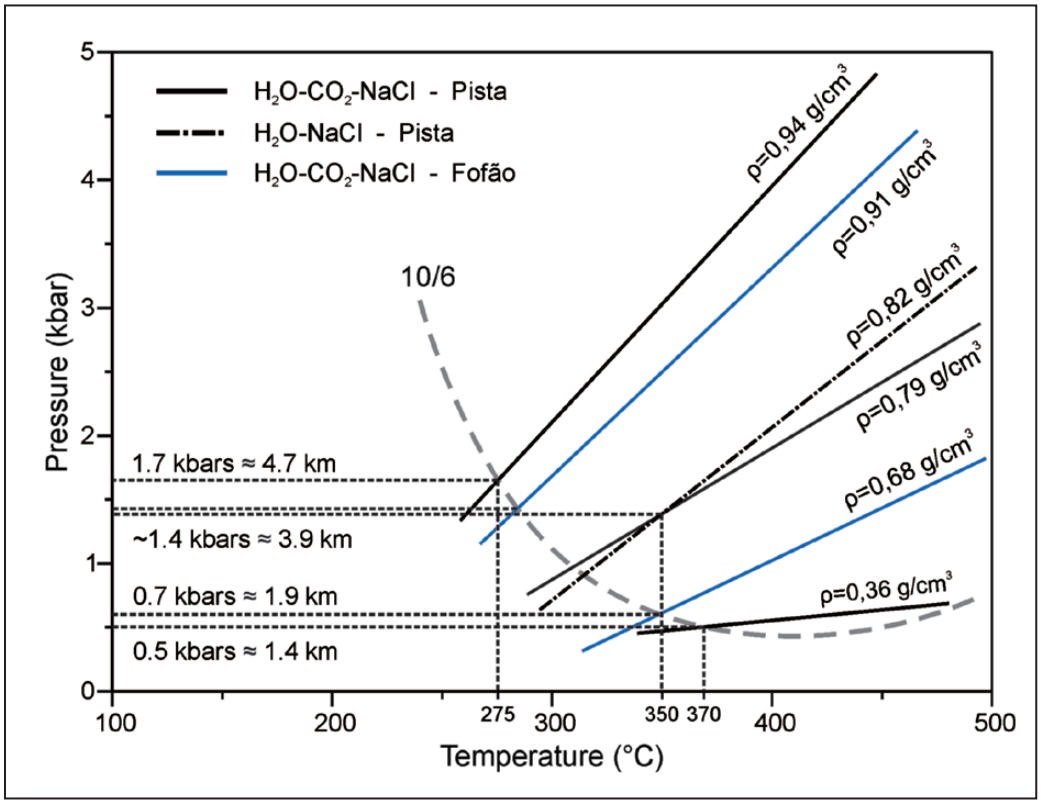

FIGURE 19. P-T diagram showing the estimated conditions for gold and metals deposition at Pista and Fofão targets. The gray dashed line represents the solvus for the CO_2-H_2O-NaCl system (10 mol% CO_2 and 6% NaCl) proposed by Bowers and Helgeson (1983).

isochores of the most representative density value for the coeval H_2O-NaCl (0.82 g/cm^3) and the mean density value of H_2O-CO_2-NaCl (0.79 g/cm^3) fluid inclusions falls above the solvus, which supports that fluid immiscibility cannot be the main mechanism for fluid entrapment (Fig. 19).

6.5. Genetic model

The genetic model for some deposits of the Tapajós Mineral Province remains controversial, and several deposits have been described as belonging to the classes of :(i) orogenic gold (Santos et al. 2001; Klein et al. 2004; Coutinho 2008; Veloso and Santos 2013), (b) granitic intrusions-related (Borges et al. 2009; Santiago et al. 2013; Villas et al. 2013; Assunção and Klein 2014; Silva Júnior and Klein 2015; Oliveira et al. 2019), (c) Au-Cu porphyry (Juliani et al. 2002; Misas 2010; Lopes and Moura 2019), and (d) epithermal (Dreher et al. 1998; Jacobi 1999; Juliani et al. 2005; Tokashiki et al. 2015). Recently, in the southeastern Tapajós Mineral Province, gold in Orosirian paleoplacer was described (Queiroz and Klein 2018).

Among the four main classes of deposits assigned to the Tapajós Mineral Province, the orogenic class is the most incompatible type for the Pista and Fofão targets because the host rocks, the hydrothermal alteration, and the mineralization differ from those typical of orogenic deposits, which are hosted mostly in metamorphic belts (Groves et al. 1998). Assuming the mineralization at Pista and Fofão as a product of a magmatic-hydrothermal system, at least three genetic models/systems can be discussed: (i) Au porphyry, (ii) intrusion-related gold, and (iii) epithermal. Regarding the porphyry system, some typical characteristics such as intense alkaline metasomatism (albite and K-feldspar hydrothermal alteration zones), the predominance of saline and hypersaline aqueous fluids (Baker 2002; Seedorf et al. 2005; Sillitoe 2010) are not observed in the two studied targets. Because they are closely related to a granitic body (Fig. 2B), the Pista and Fofão targets can be interpreted (in isolation from the others targets of Coringa deposit) as an intrusion-related deposit, but they are part of a larger magmatic-hydrothermal system hosted mainly in volcanic rocks, which is contemporaneous to a granitic body (Serra Granite), therefore not compatible with an intrusion-related system. In addition, the occurrence of base metal-rich association (Zn and Pb) in the studied targets, especially in the main ore body (Zn-Pb-Cu) (Tokashiki et al. 2015; Guimarães et al. 2015), do not favor the interpretation of the Coringa deposit as a classic intrusion related gold deposit (Baker 2002; Hart 2007), as well as the orogenic class.

The most remarkable characteristics described in the Pista and Fofão targets such as (i) the shallow volcano-plutonic association that hosts the mineralization, (ii) the quartz + adularia ± pyrite ± sericite assemblage, (iii) the polymetallic mineralization (Au, Zn, Ag, Pb, and Cu) and (iv) the presence of Ag-Au tellurides and selenides (Au-Ag affinity), are four features consistent with those of low-sulfidation epithermal deposits (Hedenquist 1987; Cooke and Simmons 2000; Sillitoe and Hedenquist 2003; Simmons et al. 2005).

Notwithstanding, these prospects show mineralogical evidence that the sulfur fugacity (fS2) has increased and reached intermediate sulfidation conditions (Sillitoe and Hedenquist 2003; Einaudi et al. 2003). The presence of manganese siderite (in breccias and veinlets) and Fe-poor sphalerite (0.16-2.96%) are some of such evidence. This sulfidation state transition has already been reported in some epithermal deposits, like in Koru and Tesbihdere mining districts (Biga Peninsula; NW Turkey) (Çiçek and Oyman 2016) and epithermal Shila-Paula gold-bearing veins (S Peru), in which adularia, Mn-silicates/carbonates, and base-metal sulfides (with small amounts of electrum) are common phases in the initial stage of hydrothermal system (Chauvet et al. 2006). Tokashiki et al. (2015) also reported this change in the sulfidation state for the Coringa deposit. In such a case, this condition may be confirmed by chemical mineral analysis in sulfides, especially in sphalerite, and in carbonates.

As regards to the fluid paleosystem, low salinity aqueous fluids predominate (<11.2 wt % NaCl equiv.) show a higher salinity than the fluids of low-sulfidation systems (0-3 wt % NaCl equiv. – Sillitoe and Hedenquist 2003), except for the deposits related to alkaline magmatism, which is not the case of the Coringa deposit (Tokashiki et al. 2015; Guimarães et al. 2015). These salinity values are more compatible with those of intermediate sulfidation systems (Sillitoe and Hedenquist 2003; Bodnar et al. 2014).

Nevertheless, some typical textural characteristics of epithermal deposits were not recognized in the studied targets, which may represent important peculiarities of these targets and/or this deposit in relation to the classic (i.e. Hedenquist 1987; Hayba 1997) and the recently studied epithermal deposits (i.e. Camprubí and Albinson 2007; Mango et al. 2014; Simpson et al. 2015). Therefore, questions about the physical and chemical conditions under which this hydrothermal paleosystem evolved remain uncertain. These include: (i) have the textures been obliterated by erosive or supergene processes, which were very intense in the Amazon region? (ii) has the crustal depth of formation of Pista and Fofão targets been deeper when compared to that of the classic epithermal deposits, which could have prevented the formation of classic epithermal textures, and, the fact that the fluid paleosystem be richer in CO_2 than most epithermal systems (Bodnar et al. 2014), which indicates a higher depth of formation? These questions indicate the need for further studies to investigate and answer them.

7. Conclusions

The geological characteristics observed in the Pista and Fofão targets, such as the: (i) shallow plutono-volcanic association of host rock; (ii) Au-Ag mineralization and metal-base (Zn, Pb, and Cu) sulfide mineral assemblages associated mainly with quartz veins in sericite rich hydrothermal alteration zones; (iii) quartz - adularia - pyrite ± sericite hydrothermal association; (iv) abundant hydrothermal alteration zones, in which, quartz - sericite - pyrite - carbonates are the main gold-related alteration zone, with distal and late and propylitic alteration indicate that the targets studied are part of a low sulfidation epithermal system. On the other hand, the presence of Mn-siderite and Fe-poor sphalerite are indicative of fluctuation in the sulfidation state of the system, which may have reached intermediate sulfidation conditions. Despite this, these targets don't show the typical textures of classical Phanerozoic epithermal deposits, it is possible that processes/genesis in the Paleoproterozoic have been some different than the modern deposits and this hypothesis need be investigated.

The paleo-fluid system is rich in low salinity aqueous fluid (up to 11.2 wt % NaCl equiv.). Despite, the initial evolution of the hydrothermal system occurred from a magmatic, low salinity CO_2-rich fluid (5.4 ± 1.3 wt % NaCl equiv.), which generates carbonic, aqueous-carbonic and part of warmer aqueous varieties (370 - 280 °C) from boiling/effervescence processes, responsible for quartz + adularia ± pyrite ± sericite paragenesis and breccias formation. The subsequent stages are marked by the influx of heated meteoric waters isothermally mixed with magmatic-derived fluids and progressive dilution, main processes that contributed to Au, Ag and base metal deposition under neutral to alkaline pH, moderately reduced, followed by increasing in fO_2 conditions, at 0.5 to 1.7 Kbar and 1.4 to 4.7 km of depth.

Acknowledgments

We thank Magellan Minerals (geologists Dennis Moore, Guillermo Hughes and Felix Huber) for the access to the data and drill cores of the Coringa Project, the support of conducting field work and sampling. We are grateful to the staff of the Microanalysis Laboratory – IG-UFPA. This paper is a contribution to the Brazilian Institute of Amazonian Geosciences (INCT GEOCIAM). ELK thanks the Brazilian CNPq-Conselho Nacional de Desenvolvimento Científico e Tecnológico for a research grant (306798/2016-6). We thank an anonymous reviewer and the Associate Editor Steffen Hagemann for the valuable comments and suggestions that allowed a significant improvement of the manuscript.

References

Assunção R.F.S., Klein E.L. 2014. The Moreira Gomes deposit of the Cuiú-Cuiú goldfield: fluid inclusions and stable isotope constraints and implications for the genesis of granite-hosted gold mineralization in the Tapajós Gold Province, Brazil. Journal of South American Earth Sciences, 49, 85-105. https://doi.org/10.1016/j.jsames.2013.11.004

Baker T. 2002. Emplacement depth and carbon dioxide-rich fluid inclusions in intrusion-related gold deposits. Economic Geology, 97(5), 1111-1117. https://doi.org/10.2113/gsecongeo.97.5.1111

Barnes H.L. 1997. Geochemistry of hydrothermal ore deposits. New York, John Wiley & Sons, 992 p.

Biondi J.C, Borgo A., Chauvet A., Monié P., Bruguier O., Ocampo R. 2018. Structural, mineralogical, geochemical and geochronological constraints on ore genesis of the gold-only Tocantinzinho deposit (Para State, Brazil). Ore Geology Reviews, 102, 154-194. https://doi.org/10.1016/j.oregeorev.2018.08.007

Bodnar R.J. 1993. Revised equation and table for freezing point depressions of H_2O-NaCl solutions. Geochimica et Cosmochimica Acta, 57(3), 683-684. https://doi.org/10.1016/0016-7037(93)90378-A

Bodnar R.J., Lecumberri-Sanchez P., Moncada D., Steele-MacInnis M. 2014. Fluid Inclusions in Hydrothermal Ore Deposits. In: Holland H. D., Turekian K. K. (eds.). Treatise on Geochemistry, Second Edition. Oxford, Elsevier, 13, 119-142. https://doi.org/10.1016/B978-0-08-095975-7.01105-0

Bodnar R.J., Reynolds T.J., Kuehn C.A. 1985. Fluid-inclusion systematics in epithermal systems. In: Berger, B. R., Bethke, P. M. (eds). Geology and Geochemistry of Epithermal Systems. Reviews in Economic Geology, Society of Economic Geologists, 2, 73-97. https://doi.org/10.5382/Rev.02.05

Borges R.M.K., Dall'agnol R., Lamarão C.N., Figueiredo M.A.B.M., Leite A.A.S., Barros C.E.M., Costi H.T. 2009. Petrografia, química mineral e processos hidrotermais associados ao depósito de ouro São Jorge, Província Aurífera do Tapajós, Cráton Amazônico. Revista Brasileira de Geociências, 39(2), 375-393. Available on line at: http://www.ppegeo.igc.usp.br/index.php/rbg/article/view/7670/7097

Borgo A., Biondi J.C., Chauvet A., Bruguier O., Monié P., Baker T., Ocampo R., Friedman R., Mortensen J. 2017. Geochronological, geochemical and petrographic constraints on the Paleoproterozoic Tocantinzinho gold deposit (Tapajos Gold Province, Amazonian Craton - Brazil): Implications for timing, regional evolution and deformation style of its host rocks. Journal of South American Earth Sciences, 75, 92-115. https://doi.org/10.1016/j.jsames.2017.02.003

Borisenko A.S. 1977. Study of the salt composition of solutions in gas-liquid inclusions in minerals by the cryometric method. Soviet Geology and Geophysics, 18, 11-19.

Bowers T.S., Helgeson H.C. 1983. Calculation of the thermodynamic and geochemical consequences of non-ideal mixing in the system H_2O-CO_2-NaCl on phase relations in geological systems: equation of state for H_2O-CO_2-NaCl fluids at high pressures and temperatures. Geochimica et Cosmochimica Acta, 47, 1247-1275.

Brown P.E. 1989. Flincor: a microcomputer program for the reduction and investigation of fluid-inclusion data. American Mineralogist, 74(11-12), 1390-1393.

Brown P.E., Lamb W.M. 1986. Mixing of H_2O e CO_2 in fluid inclusions: geobarometry and Archean gold deposits. Geochimica et Cosmochimica Acta, 50(5), 847-852. https://doi.org/10.1016/0016-7037(86)90360-1

Camprubí A., Albinson T. 2007. Epithermal deposits in México - Update of current knowledge, and an empirical reclassification. In: Alaniz-Álvarez S.A., Nieto-Samaniego Á.F. (eds.). Geology of México: Celebrating the Centenary of the Geological Society of México. GSA Special Papers, 422, 377-415. https://doi.org/10.1130/2007.2422(14)

Cassini L.V, Juliani C., Gutierrez D.F.G. 2017. O Sistema Hidrotermal do Patrocínio, Província Mineral do Tapajós (PA): Petrografia, Geoquímica e Idades U-Pb. In: Lima A.M.M., Gorayeb P.S.S. (orgs). Contribuições à Geologia da Amazônia. Belém, SBG, 10, 109-125.

Chauvet A., Bailly L., André A.S., Monié P., Cassard D., Tajada F.L., Vargas J.R., Tuduri J. 2006. Internal vein texture and vein evolution of the epithermal Shila-Paula district, southern Peru. Mineralium Deposita, 41, 387-410. https://doi.org/10.1007/s00126-006-0068-4

Chi G.X., Lu H.Z. 2008. Validation and representation of fluid inclusion microthermometric data using the fluid inclusion assemblage (FIA) concept. Acta Petrologica Sinica, 24(9), 1945-1953.

Çiçek M., Oyman T. 2016. Origin and evolution of hydrothermal fluids in epithermal Pb-Zn-Cu ± Au ± Ag deposits at Koru and Tesbihdere mining districts, Çanakkale, Biga Peninsula, NW Turkey. Ore Geology Reviews, 78, 176-195. https://doi.org/10.1016/j.oregeorev.2016.03.020

Collins P.L.F. 1979. Gas hydrates in CO2-bearing fluid inclusions and the use of freezing data for estimation of salinity. Economic Geology, 74, 1435-1444.

Cooke D.R., Simmons S.F. 2000. Characteristics and genesis of epithermal gold deposits. In: Hagemann S.G., Brown P.E. Gold in 2000. Reviews in Economic Geology, 13, 221-244. https://doi.org/10.5382/rev.13.06

Corrêa Lima R.G., Klein E.L., Borges R.M.K., Oliveira H.T., Feio J.V.B. 2014. Petrografia e alteração hidrotermal no Alvo Pista, Depósito Coringa, Província Aurífera do Tapajós, Pará. In: Congresso Brasileiro de Geologia, 47.

Coutinho M.G.N. 2008. Província Mineral do Tapajós: geologia, metalogenia e mapa previsional para ouro em SIG. Rio de Janeiro, CPRM, 420 p.

Dilles J.H., Einaudi M.T. 1992. Wall-rock alteration and hydrothermal flow paths about the Ann-Mason porphyry copper deposit, Nevada; a 6-km vertical reconstruction. Economic Geology, 87(8), 1963-2001. https://doi.org/10.2113/gsecongeo.87.8.1963

Dong G., Morrison G.W. 1995. Adularia in epithermal veins, Queensland: morphology, structural state and origin. Mineralium Deposita, 30, 11-19. https://doi.org/10.1007/BF00208872

Dreher A.M., Vlach S.R.F., Martini S.L. 1998. Adularia associated with epithermal gold veins in the Tapajós Mineral Province, Pará State, Northern Brazil. Revista Brasileira de Geociências, 28(3), 397-404. https://doi.org/10.25249/0375-7536.1998397404

Dzick W.A. 2015. Coringa mineral resource NI 43-101 technical report: project n. V1491. Vancouver, Snowden. Available online at: https://anfieldgold.com/projects/technical-reports / (accessed on 08 march 2016).

Einaudi M.T., Hedenquist J.W., Inan E.E. 2003. Sulfidation state of fluids in active and extinct hydrothermal systems: transitions from porphyry to epithermal environments. In: Simmons S.F., Graham I. (eds.). Volcanic, Geothermal, and Ore-Forming Fluids: Rulers and Witnesses of Processes within the Earth. Littleton, Society of Economic

Geologists. Special Publication, 10, 285-313. https://doi.org/10.5382/SP.10.15

Feio J.V.B. 2014. Petrografia das rochas hospedeiras e do minério aurífero e estudo de isótopos de chumbo no alvo Mato Velho, SE da Província Aurífera do Tapajós, Pará. Graduation Work. Instituto de Geociências, Universidade Federal do Pará, Belém, 71 p.

Goldstein R.H., Reynolds T.J. 1994. Systematics of fluid inclusions in diagenetic minerals. SEPM Short Course 31, 199. https://doi.org/10.2110/scn.94.31

Groves D. I., Goldfarb R. J., Gebre-Mariam M., Hagemann S. G., Robert, F. 1998. Orogenic gold deposits: A proposed classification in the context of their crustal distribution and relationship to other gold deposit types. Ore Geology Review, 13(1-5), 7-27. https://doi.org/10.1016/S0169-1368(97)00012-7

Guimarães S.B., Klein E.L., Chaves C.L., Souza S.M., Castro J.M.R., Queiroz J.D.S., Feio J.V.B., Correa Lima R.G. 2015. Metalogenia das Províncias Minerais do Brasil: Área sudeste do Tapajós, Estado do Pará. Informe de Recursos Minerais, Série Províncias Minerais do Brasil, n. 3. Programa Geologia do Brasil. Brasília, CPRM, 61 p. Available online at: http://rigeo.cprm.gov.br/jspui/handle/doc/16601 / (accessed on 22 Jul 2016).

Guimarães S.B., Klein E.L., Correa R.T. 2019. Reassessment of the geology of the southeastern Tapajós Gold Province, Amazonian Craton, Brazil, based on field, petrographic, and airborne geophysical data. Journal of the Geological Survey of Brazil, 2(1), 1-16. https://doi.org/10.29396/jgsb.2019.v2.n1.1

Gunnesh K., Samari H., Harvey T., Breckenridge L. 2019. NI 43-101 Technical report of Coringa Gold Project, Brazil. Mineral Resource Estimate. Available on line at: https://www.serabigold.com/wp-content/uploads/2018/02/Coringa-FS-43-101.pdf (accessed on 26 June 2019)

Hart C.J.R. 2007. Reduced intrusion-related gold deposits. In: Good fellow, W.D. (ed.). Mineral Deposits of Canada. Geological Association of Canada,. Special Publication, 5, 5-112.

Hayba D.O. 1997. Environment of ore deposition in the Creede mining district, San Juan Mountains, Colorado: Part V, Epithermal mineralization from mixing in the OH vein. Economic Geology, 92(1), 29-44. http://dx.doi.org/10.2113/gsecongeo.92.1.29

Hayba D.O., Bethke P.M., Heald P., Foley N.K. 1985. Geologic, mineralogic, and geochemical characteristics of volcanic-hosted epithermal precious metal deposits. In: Berger B. R., Bethke P. M (eds.). Geology and Geochemistry of Epithermal Systems. Reviews in Economic Geology, 2, 129-167. https://doi.org/10.5382/Rev.02.07

Heald P., Foley N.K., Hayba D.O. 1987. Comparative anatomy of volcanic-hosted epithermal deposits: Acid-sulfate and adularia-sericite types. Economic Geology, 82(1), 1-26. https://doi.org/10.2113/gsecongeo.82.1.1

Hedenquist J.W. I987. Mineralization associated with volcanic-related hydrothermal systems in the Circum-Pacific Basin. In: Horn M.K. (ed.). Circum Pacific Energy and Mineral Resources Conference, 4, 513-524.

Hedenquist J.W., Arribas A., Jr., Gonzalez-Urien E. 2000. Exploration for epithermal gold deposits. In: Hagemann S.G., Brown P.E. Gold in 2000. Reviews in Economic Geology, 13, 245-277. https://doi.org/10.5382/Rev.13.07

Hedenquist J.W., Lindqvist W.P. 1985. Aspects of gold geology and geochemistry. Townsville, James Cook University of North Queensland, Dept. of Geology, Economic Geology Research Unit. Contributions of the Economic Geology Research Unit, 23.

Jacobi P. 1999. The discovery of epithermal Au-Cu-Mo proterozoic deposits in the Tapajós Province, Brazil. Revista Brasileira de Geociências, 29(2), 277-279.

Jébrak M. 1997. Hydrothermal breccias in vein-type ore deposits: a review of mechanisms, morphology and size distribution. Ore Geology Reviews, 12(3), 111-134. https://doi.org/10.1016/S0169-1368(97)00009-7

Juliani C., Correa-Silva R.H., Monteiro L.V.S., Bettencourt J.S., Nunes C.M.D. 2002. The Batalha Au-Granite system e Tapajós Province, Amazonian Craton, Brazil: hydrothermal alteration and regional implication. Precambrian Research, 119(1-4), 225-256. https://doi.org/10.1016/S0301-9268(02)00124-9

Juliani C., Rye R.O., Nunes C.M.D., Snee L.W., Silva R.H.C., Monteiro L.V.S., Bettencourt J.S., Neumann R., Alcover Neto A. 2005. Paleoproterozoic high-sulfidation mineralization in the Tapajós gold province, Amazonian Craton, Brazil: geology, mineralogy, alunite argon age, and stable isotope constraints. Chemical Geology, 215(1-4), 95-125. https://doi.org/10.1016/j.chemgeo.2004.06.035

Juliani C., Carneiro C.C., Carreiro-Araújo S.A., Fernandes C.M.D., Monteiro L.V.S., Crósta A.P. 2013. Estruturação dos arcos magmáticos paleoproterozoicos na porção sul do Cráton Amazônico: implicações geotectônicas e metalogenéticas. In: Simpósio de Geologia da Amazônia, 13, 157-160.

Juliani C., Vasquez M.L., Klein E.L., Villas R.N., Misas C.M.E., Santiago E.S.B., Monteiro L.V.S., Carneiro C.C., Fernandes C.M.D., Usero G. 2014. Metalogenia da Província Tapajós. In: Silva M.G.; Rocha Neto, M. B., Jost H.; Kuyumajian R.M. (org.). Metalogênese das províncias tectônicas brasileiras. Belo Horizonte, CPRM, p. 51-90. Available on line at: http://rigeo.cprm.gov.br/jspui/handle/doc/19389

Klein E.L., Vasquez M.L., Rosa-Costa L.T., Carvalho J.M.A. 2002. Geology of Paleoproterozoic gneiss and granitoid-hosted gold mineralization in Southern Tapajós Gold Province, Amazonian Craton, Brazil. International Geology Review, 44(6), 544-558. https://doi.org/10.2747/0020-6814.44.6.544

Klein E.L., Rosa-Costa L.T., Carvalho J.M.A. 2004. Estudo de inclusões fluidas em veio de quartzo aurífero do prospecto Patinhas, Província Aurífera do Tapajós, Cráton Amazônico. Revista Brasileira de Geociências, 34(1), 59-66.

Klein E.L., Carvalho J.M.A. 2008. Recursos Minerais. In: Vasquez M.L., Rosa-Costa L.T. (eds.). Geologia e Recursos Minerais do Estado do Pará: texto explicativo do mapa geológico e de recursos minerais do estado do Pará, Escala 1:1.000.000. Belém, CPRM. p. 217-262. Available on line at: http://rigeo.cprm.gov.br/jspui/handle/doc/10443

Klein E.L., Almeida M.E., Rosa-Costa L.T. 2012. The 1.89-1.87 Ga Uatumã Silicic Large Igneous Province, northern South America. Large Igneous Provinces Commission. Available on line at: http://www.largeigneousprovinces.org / (accessed on 09 May 2015)

Klein E.L., Rodrigues J.B., Queiroz J.D.S., Oliveira R.G., Guimarães S.B., Chaves C.L. 2017. Deposition and tectonic setting of the Palaeoproterozoic Castelo dos Sonhos metasedimentary formation, Tapajós Gold Province, Amazonian Craton, Brazil: age and isotopic constraints. International Geology Review, 59(7), 864-883. https://doi.org/10.1080/00206814.2016.1237311

Klein E.L., Guimarães S.B., Rodrigues J.B., Chaves C.L., Souza-Gaia S.M., Lopes E.C., Castro J.M.E. 2018. The Novo Progresso Formation, Tapajós Gold Province, Amazonian Craton: zircon U-Pb and Lu-Hf constraints on the maximum depositional age, reconnaissance provenance study, and tectonic implications. Journal of the Geological Survey of Brazil, 1(1), 31-42. https://doi.org/10.29396/jgsb.2018.v1.n1.3.

Lafon J.M., Coutinho M.G.N. 2008. Isótopos radiogênicos de chumbo. In: Coutinho, M.G.N. (ed.). Província Mineral de Tapajós: geologia, metalogenia e mapa previsional para ouro em SIG: texto, mapas e SIG. Rio de Janeiro, CPRM. p. 251-262. Available on line at: http://rigeo.cprm.gov.br/jspui/handle/doc/1208

Lamarão C.N., Dall'Agnol R., Lafon J.M., Lima E.F. 2002. Geology, geochemistry and Pb-Pb zircon geochronology of the Paleoproterozoic magmatism of Vila Riozinho, Tapajós Gold Province Amazonian Craton, Brazil. Precambrian Research, 119(1-4), 189-223. https://doi.org/10.1016/S0301-9268(02)00123-7

Leach T., Corbett G. 2008. Fluid Mixing as a Mechanism for Bonanza Grade Epithermal Gold Formation. In: Terry Leach Symposium, 48, 83-92.

Lopes A.A.C., Moura M.A. 2019. The Tocantinzinho Paleoproterozoic Porphyry-Style Gold Deposit, Tapajós Mineral Province (Brazil): Geology, Petrology and Fluid Inclusion Evidence for Ore-Forming Processes. Minerals, 9(1), 29. https://doi.org/10.3390/min9010029

Mango H., Arehart G., Oreskes N., Zantop H. 2014. Origin of epithermal Ag–Au–Cu–Pb–Zn mineralization in Guanajuato, Mexico. Mineralium Deposita, 49, 119-143. https://doi.org/10.1007/s00126-013-0478-z

Misas C.M.E. 2010. Geologia e gênese do depósito de Au-(Cu) do Palito, Província Aurífera do Tapajós. MSc Dissertation, Instituto de Geociências, Universidade de São Paulo, São Paulo, 235 p.

Moncada D., Mutchler S., Nieto A., Reynolds T.J., Rimstidt J.D., Bodnar R.J. 2012. Mineral textures and fluid inclusion petrography of the epithermal Ag–Au deposits at Guanajuato, Mexico: application to exploration. Journal of Geochemical Exploration, 114, 20-35. https://doi.org/10.1016/j.gexplo.2011.12.001

Oliveira H.T., Borges R.M.K., Klein E.L., Lamarão C.N., Marques G.T., Corrêa Lima R.G. 2019. Alteração hidrotermal e fluidos mineralizantes no alvo Jerimum de Baixo, Campo Mineralizado do Cuiú-Cuiú,

Província Aurífera do Tapajós: um estudo baseado em petrografia, inclusões fluidas e química mineral. Geologia USP, Série Científica, 19(1), 3-32. http://dx.doi.org/10.11606/issn.2316-9095.v19-142134

Pirajno F. 1992. Hydrothermal mineral deposits. Principles and fundamental concepts for the exploration geologists. Berlin, Springer-Verlag, 709 p. https://doi.org/10.1007/978-3-642-75671-9

Pirajno F. 2009. Hydrothermal Processes and Mineral Systems. New York, Springer-Verlag, 1250 p. https://doi.org/10.1007/978-1-4020-8613-7

Pollard P.J. 1983. Magmatic and postmagmatic processes in the formation of rocks associated with rare element deposits. Transactions of the Institution of Mining and Metallurgy, 92, B1-9.

Queiroz J.D.S., Villas R.N.N. 2015. Estudo dos fluidos hidrotermais relacionados ao depósito Tocantinzinho, Província Aurífera do Tapajós (PA), com base em inclusões fluidas. In: Gorayeb P.S.S., Lima A.M.M. (orgs). Contribuições à Geologia da Amazônia. Belém, SBG, 9, 93-117.

Queiroz J.D.S., Klein E.L., Rodrigues J.B. 2015. Rochas intrusivas na Formação Castelo dos Sonhos, Cráton Amazônico: petrografia, geocronologia, geoquímica e implicações para as idades de sedimentação e da mineralização no depósito aurífero Castelo de Sonhos. Boletim do Museu Paraense Emílio Goeldi, Ciências Naturais, 10(3), 341-380.

Queiroz J.D.S., Klein E.L. 2018. The Paleoproterozoic metaconglomerate-hosted Castelo de Sonhos gold deposit, Tapajós Gold Province, Amazonian Craton: a modified paleoplacer origin. Journal of the Geological Survey of Brazil, 1(2), 81-99. https://doi.org/10.29396/jgsb.2018.v1.n2.3

Ramboz C., Pichavant M., Weisbrod A. 1982. Fluid immiscibility in natural processes: use and misuse of fluid inclusion data. II. Interpretation of fluid inclusion data in terms of immiscibility. Chemical Geology, 37(1-2), 29-48. https://doi.org/10.1016/0009-2541(82)90065-1

Reed M.H. 1997. Hydrothermal alteration and its relationship to ore fluid composition. In: Barnes H.L. (ed.). Geochemistry of hydrothermal ore deposits. New York, John Wiley & Sons. p. 303-365.

Robb L. 2006. Introduction to ore-forming processes. Australia, Blackwel Publishing, 373 p.

Roedder E. 1984. Fluid Inclusions. Virginia, Mineralogical Society of America. Reviews in Mineralogy, 12, 644 p.

Santiago E.S.B., Villas R.N., Ocampo R.C. 2013. The Tocantinzinho gold deposit, Tapajós Province, State of Pará: host granite, hydrothermal alteration and mineral chemistry. Brazilian Journal of Geology, 43(1), 185-208.

Santos J.O.S., Groves D.I., Hartmann L.A., Moura M.A., McNaughton N.J. 2001. Gold deposits of the Tapajós and Alta Floresta Domains, Tapajós–Parima orogenic belt, Amazon Craton, Brazil. Mineralium Deposita, 36, 453-488. https://doi.org/10.1007/s001260100172

Santos J.O.S., Hartmann L.A., Gaudette H.E., Groves D.I., Almeida M.E., McNaughton N.J., Fletcher I.R. 2000. A new understanding of the provinces of the Amazon Craton based on integration of field mapping and U-Pb and Sm-Nd geochronology. Gondwana Research, 3(4), 453-488. https://doi.org/10.1016/S1342-937X(05)70755-3

Santos J.O.S., Hartmann L.A., McNaughton N.J., Fletcher I.R. 2002. Timing of mafic magmatism in the Tapajós Province (Brazil) and implication for the evolution of the Amazon Craton: evidence from baddeleyite and zircon U-Pb SHRIMP geochronology. Journal of South American Earth Sciences, 15(4), 409-429. https://doi.org/10.1016/S0895-9811(02)00061-5

Santos J.O.S., Rizzotto G.J., Potter P.E., McNaughton N.J., Matos R.S., Hartmann L.A., Chemale F., Quadros M.E.S. 2008. Age and autochthonous evolution of the Sunsás Orogen in West Amazon Craton based on mapping and U-Pb geochronology. Precambrian Research, 165(3-4), 120-152. https://doi.org/10.1016/j.precamres.2008.06.009

Santos J.O.S., Van Breemen O.T., Groves D.I., Hartmann L.A., Almeida M.E., McNaughton N.J., Fletcher I.R. 2004. Timing and evolution of multiple Paleoproterozoic magmatic arcs in the Tapajós Domain, Amazon Craton: constraints from SHRIMP and TIMS zircon, baddeleyite and titanite U-Pb geochronology. Precambrian Research, 131(1-2), 73-109. https://doi.org/10.1016/j.precamres.2004.01.002

Santos M.D., Aquino L.B.M., Serra V.F.H., Lima M.V.G.R., Galarza M.A., Lafon J.M. 2013. Geocronologia das rochas hospedeiras e do minério com implicações na gênese do depósito aurífero palito, Província Tapajós, sudoeste do Pará. In: Simpósio de Geologia da Amazônia, 13, 702-704.

Santos R.A., Coutinho M.G.N. 2008. Geologia estrutural. In: Coutinho, M. G. N. (ed.). Província Mineral do Tapajós: geologia, metalogenia e mapa previsional para ouro em SIG. Rio de Janeiro, CPRM. p. 97-135.

Saunders J.A., Hofstra A.H., Goldfarb R.J., Reed M.H. 2014. Geochemistry of Hydrothermal Gold Deposits. In: Holland, H. D., Turekian, K. K. (eds.). Treatise on Geochemistry. Oxford, Elsevier. p. 383-424.

Seedorf E., Dilles J.H., Proffett Jr. J.M., Eunadi M.T., Zurcher L., Stavast W.J.A., Johnson D.A., Barton M.D. 2005. Porphyry deposits: characteristics and origin of hypogene features. In: Hedenquist, J. W., Thompson, J. F. H., Goldfarb, R. J.; Richards, J. P. (ed.). Economic geology 100th anniversary volume (1905-2005). Littleton, Society of Economic Geologists. p. 251-298.

Sheppard S.M.F., Nielsen R.L., Taylor H.P.Jr. 1971. Hydrogen and oxygen isotope ratios in minerals from porphyry copper deposits. Economic Geology, 66(4), 515-542. https://doi.org/10.2113/gsecongeo.66.4.515

Sillitoe R.H. 2010. Porphyry copper systems. Economic Geology, 105(1), 3-41. https://doi.org/10.2113/gsecongeo.105.1.3

Sillitoe R.H., Hedenquist J.W. 2003. Linkages between Volcanotectonic Settings, ore-Fluid Compositions, and Epithermal Precious Metal Deposits. In: Simmons S.F., Graham, I. (eds.). Volcanic, Geothermal, and Ore-Forming Fluids: Rulers and Witnesses of Processes Within the Earth. Society of Economic Geologists. Special Publication, 10, 315-343.

Silva Júnior C.A.S., Klein E.L. 2015. Geologia e características do fluido mineralizador dos alvos auríferos Jerimum de Cima e Babi, campo mineralizado do Cuiú-Cuiú, Província Aurífera do Tapajós, Cráton Amazônico, com base em estudos de inclusões fluidas e de isótopos estáveis. Boletim do Museu Paraense Emílio Goeldi, Ciências Naturais, 10(2), 105-136.

Simmons S., White N., John D.A. 2005. Geological Characteristics of Epithermal Precious and Base Metal Deposits. In: Hedenquist J.W., Thompson J.F.H., Goldfarb R.J., Richards J.P. (eds.). Economic Geology: One Hundredth Anniversary Volume 1905–2005. Ottawa, Economic Geology Department of Earth Sciences University of p. 485-522. https://doi.org/10.5382/AV100.16

Simpson M.P., Strmic Palinkas S., Mauk J.L., Bodnar R.J. 2015. Fluid inclusion chemistry of adulariasericite epithermal Au-Ag deposits of the southern Hauraki Goldfield, New Zealand. Economic Geology, 110(3), 763-786. https://doi.org/10.2113/econgeo.110.3.763

Skinner B.J. 1997. Hydrothermal mineral deposits: what we do and don't know. In: Barnes H.L. (ed.). Geochemistry of Hydrothermal Ore Deposits. 3. ed. New York, John Wiley & Sons. p. 1-29.

Souza S.R.C. 2009. Petrografia, Litogeoquímica, Geocronologia e Geoquímica Isotópica da Mineralização Aurífera e Rochas Hospedeiras do Prospecto Água Branca, Província Tapajós. MSc Dissertation, Instituto de Geociências, Universidade de Brasília, Brasília, 106 p.

Teixeira N.A., Matos F.M.V., Ganade C.E., Klein E.L., Dreher A.M., Tavares F.M., Campos L.D., Porto F. 2015. Carajás and Tapajós mineral Provinces: Cratonic and Pericratonic Lithosphere Keel Metallogeny. In: Simpósio de Geologia da Amazônia, 14, 404-407.

Tokashiki C.C., Juliani C., Monteiro L.V.S., Misas C.M.E., Aguja M.A., Arrais L.B. 2015. Eventos vulcânicos de 1,97 Ga com mineralizações de ouro epitermais low- e intermediate-sulfidation na porção sul da Província Mineral do Tapajós (PA). In: Gorayeb P.S.S, Lima A.M.M. (orgs). Contribuições à Geologia da Amazônia. Belém, SBG, 9, 67-84.

Vasquez M.L., Ricci P.S.F., Klein E.L. 2002. Granitoides pós-colisionais da porção leste da Província Tapajós. In: Klein E.L., Vasquez M.L., Rosa-Costa L.T. (orgs). Contribuições à Geologia da Amazônia. Belém, SBG, 3, p. 119-138.

Vasquez M.L., Rosa-Costa L.T., Silva C.M.G., Klein E.L. 2008. Compartimentação tectônica. In: Vasquez M.L., Rosa-Costa L.T. (orgs). Geologia e Recursos Minerais do Estado do Pará: texto explicativo do mapa geológico e de recursos minerais do estado do Pará, Escala 1:1.000.000. Belém, CPRM. p. 39-112. Available on line at: http://rigeo.cprm.gov.br/jspui/handle/doc/10443

Vasquez M.L., Chaves C.L., Moura E.M., Oliveira J.K.M., Lafon J.M. 2013. Eventos magmáticos de 2020 - 1980 Ma nas folhas são domingos e jardim do ouro, porção leste do domínio tapajós. In: Simpósio de Geologia da Amazônia, 13, 209-212.

Vasquez M.L., Chaves C.L., Moura E.M., Oliveira J.K.M. 2014. Folha SB.21-Z-A-III Jardim do Ouro: carta geológica, Escala 1:100.000. Programa Geologia do Brasil. Belém, CPRM. Available on line

at: http://rigeo.cprm.gov.br/jspui/bitstream/doc/17997/6/carta_geologica_jardim_ouro.pdf

Vasquez M.L., Chaves C.L., Moura E.M., Oliveira J.K.M. 2019. Idades U-Pb por LA-ICP-MS em zircão das rochas do Grupo Jacareacanga, Sudoeste do Domínio Tapajós. In: Simpósio de Geologia da Amazônia, 16.

Veloso A.S.R., Santos M.D. 2013. Geologia, petrografia e geocronologia das rochas do depósito aurífero Ouro Roxo, Província Tapajós, Jacareacanga (PA), Brasil. Brazilian Journal of Geology, 43(1), 22-36. http://dx.doi.org/10.5327/Z2317-48892013000100004

Villas R.N.N., Santiago E.S.B., Castilho M.P. 2013. Contexto geológico, estudos isotópicos (C, O e Pb) e associação metálica do depósito aurífero Tocantinzinho, DomínioTapajós, Província Tapajós-Parima. Geologia USP, Série Científica, 13(1), 111-138. https://doi.org/10.5327/Z1519-874X2013000100008

White N.C., Hedenquist J.W. 1995. Epithermal gold deposit: styles, characteristics and exploration. SEG Newsletter, 23, 1-9.

Wilkinson J.J. 2001. Fluid inclusion in hydrothermal ore deposit. Lithos, 55(1-4), 229-272. https://doi.org/10.1016/S0024-4937(00)00047-5